# Phase-field modeling of epitaxial growth of polycrystalline quartz veins in hydrothermal experiments

F. WENDLER[1], A. OKAMOTO[2] AND P. BLUM[1]

[1]*Institute for Applied Geosciences (AGW), Karlsruhe Institute of Technology (KIT), Karlsruhe, Germany;* [2]*Graduate School of Environmental Studies, Tohoku University, Aramaki Aoba-ku, Sendai, Japan;*

## ABSTRACT

Mineral precipitation in an open fracture plays a crucial role in the evolution of fracture permeability in rocks, and the microstructural development and precipitation rates are closely linked to fluid composition, the kind of host rock as well as temperature and pressure. In this study, we develop a continuum thermodynamic model to understand polycrystalline growth of quartz aggregates from the rock surface. The adapted multiphase-field model takes into consideration both the absolute growth rate as a function of the driving force of the reaction (free energy differences between solid and liquid phases), and the equilibrium crystal shape (Wulff shape). In addition, we realize the anisotropic shape of the quartz crystal by introducing relative growth rates of the facets. The missing parameters of the model, including surface energy and relative growth rates, are determined by detailed analysis of the crystal shapes and crystallographic orientation of polycrystalline quartz aggregates in veins synthesized in previous hydrothermal experiments. The growth simulations were carried out for a single crystal and for grain aggregates from a rock surface. The single crystal simulation reveals the importance of crystal facetting on the growth rate; for example, growth velocity in the *c*-axis direction drops by a factor of ~9 when the faceting is complete. The textures produced by the polycrystal simulations are similar to those observed in the hydrothermal experiments, including the number of surviving grains and crystallographic preferred orientations as a function of the distance from the rock wall. Our model and the methods to define its parameters provide a basis for further investigation of fracture sealing under varying conditions.

Key words: numerical modeling, phase-field model, polycrystalline growth, quartz growth, quartz vein

Received 25 March 2014; accepted 10 April 2015

Corresponding author: Frank Wendler, Institute for Applied Geosciences (AGW), Karlsruhe Institute of Technology (KIT), Kaiserstraße 12, 76131 Karlsruhe, Germany.
Email: frank.wendler@kit.edu. Tel: +49 721 608 43336. Fax: +49 721 606 279.
Present address: Frank Wendler, Institute of Microstructure Technology (IMT), Karlsruhe Institute of Technology (KIT), Postfach 3640, D-76021 Karlsruhe, Germany

## INTRODUCTION

Deformation and fluid flow processes in the earth's crust are closely linked – a key element of many problems with wide scientific and economic impact, as geohazards, the recovery of hydrocarbons, geothermal energy, $CO_2$ sequestration, and the storage of hazardous waste. This coupling leads to cyclic changes in the rock's strength and recurrent permeability-creating and permeability-destroying processes like crack sealing by mineral precipitation at the fracture walls (Holland & Urai 2010). The nature of fluid flow – continuous flow or episodic flow through fracture networks – depends on crustal deformation mechanism, fluid source, lithostatic stress, fluid pressure, temperature, and rock strength (Oliver 1996; Blum *et al.* 2005, 2009; Cox 2005).

Tectonic mineral veins bear the traces of former deformation, fracturing, and fluid-transport processes and constitute a record of the complex geochemical, hydraulic, and mechanical history of the rock. For example, a sporadic or cyclic reopening of completely or partially sealed veins may occur, as proposed for the crack-sealing process (Ramsay 1980). In growing antitaxial veins, new material is accumulated at the boundary of the initial crack and the growing vein crystals, which follow the trajectory of the opening crack, whereas in syntaxial veins, sealing starts from the fracture surfaces and propagates to the inside of the crack (Durney & Ramsay 1973). According to their microstructural

evolution during crystal growth, four major types of veins have been identified (e.g. Bons 2000; Oliver & Bons 2001; Bons *et al.* 2012). *Fibrous veins* are composed of grains with very large length to width ratios, often separated by curved boundaries (Hilgers *et al.* 2001). It was proposed that they form by a pressure dissolution–precipitation mechanism (Oliver & Bons 2001), involving diffusive transport from nearby rock or assuming cyclic crack sealing with very small crack increments (Cox & Etheridge 1983; Urai *et al.* 1991; Fisher & Brantley 1992). Veins with *elongate-blocky* microstructure are assumed to result from growth competition between grains starting as epitaxial overgrowths of rock wall grains (Bons 2000). Here, larger crack aperture leads to the development of crystal facets, that is euhedral crystal terminations at the liquid interface. *Stretched crystal veins* are composed of grains with serrated boundaries bridging the whole distance between both sides of an original fracture. They are supposed to form by continuous crack sealing, where rock wall material and fluid inclusions mark former vein–rock boundaries (Bons 2000). Veins filled with grains showing no signs of directional growth are termed '*blocky veins*', and a mechanism of homogeneous nucleation and free growth following the fracture opening was proposed (Okamoto & Tsuchiya 2009).

Experimental studies under well-defined conditions are essential to test these models, but are rare in the literature. Lee *et al.* (1996) and Lee & Morse (1999) studied calcite growth in a synthetic unitaxial vein of 10 cm length and 2-mm aperture with a single Iceland spar crystal as substrate. Under laminar flow calcite crystals started growing from micron-sized, isolated seeds, forming aggregates of 30 to 60 μm diameter without well-defined facets in 1 month. The authors concluded that either very high flow velocities or low supersaturations are necessary to completely seal larger portions of a vein. Hilgers and coworkers published several studies using the cubic mineral alum as a vein filling analogue in a transparent flow-through cell with mm-sized gap (Hilgers & Urai 2002; Hilgers *et al.* 2004; Nollet *et al.* 2006). At the upstream inlet of the channel, the precipitation rate was higher and leads to punctual sealing during the late stage, where individual crystals dominated the remaining flow path. Observable difference in material precipitation occurs on lengths of several 100 m (Hilgers *et al.* 2004). Hydrothermal sealing of micro-fractures of 10–20 μm width under strong uniaxial compression and confinement pressure was observed by Hilgers & Tenthorey (2004). However, no details on the flow or growth mechanism during sealing were provided. Flow-through hydrothermal experiments with apertures of ~300 μm under-defined (p, T, c) conditions were carried out recently by Okamoto *et al.* (2010) and Okamoto & Sekine (2011) for different quartz rocks. These well-controlled experiments are used in the present

study for calibration and evaluation of the numerical simulations.

Numerical models are useful for unraveling the relationship between the microstructural pattern and the transport process. They can help to quantify timing of vein closure and predict temperature, composition, and pressure of the mineralizing fluid. To date, numerical models have required simplifications to reduce the complexity of the physico-chemical processes. A purely kinetic approach with an orientation-dependent growth-rate function was used in the *vein-growth* model by Bons (2001). It takes into account crystal symmetry and represents interfaces as discrete line segments. For antitaxial growth, growth competition and tracking of grains at rock wall asperities were simulated (Hilgers *et al.* 2001; Nollet *et al.* 2005), deformation-related fibrous growth (Koehn *et al.* 2001) and zeolite growth (Bons & Bons 2003). The simulation software *prism3D* is based on a cellular automaton model and has been applied to study diagenetic pore-scale mineralization processes in quartz (Lander *et al.* 2008) and carbonate rock (Gale *et al.* 2010). Although only a limited set of grain orientations is used, differentiation between slow kinetics of facets and fast growth of nonfacet orientations is captured and explains experimentally observed features such as nucleation discontinuities. On the other hand, reactive transport models incorporate processes, which are specific to the mineral system under consideration like diffusion, advection, heat transport and include chemical reactions (e.g. Steefel *et al.* 2005), and have been successfully applied to model isotropic mineral growth (Li *et al.* 2008; Yoon *et al.* 2012); however, they do not account for crystalline anisotropy and polycrystalline fabric. Hence, on the microstructural scale, they can be applied up to date successfully for nearly isotropic mineral growth.

Phase-field models (PFMs) have become standard tools to describe microstructure evolution in materials science, and in addition to diffusive- and fluid transport can capture multicomponent phase transitions and kinetics of crystal interfaces (Hecht *et al.* 2004). In contrast to finite element approaches, the PFM relies on a partitioning of space into domains with nonzero interface thickness. It offers a convenient way to integrate thermodynamics of bulk phases and interfaces within a single kinetic approach, but needs a precise input for the related parameters (Moelans *et al.* 2008). Previously, Hubert *et al.* (2009) used a PFM with orientation parameter and diffusion-limited growth process for 10 grains in 2D. The results were qualitative, as no parameters adapted to a real mineral system were used. Morphologic evolution with several hundreds of crystals in 2D and 3D was obtained for zeolite thin films (Wendler *et al.* 2011), where thermodynamic data were used to generate the driving forces. The observed crystal shape was modeled separately via anisotropy of surface energy and kinetics, but no major difference was found. Polycrystalline

growth of the mineral alum (KAl(SO4)$_2$·12H$_2$O) was simulated with a PFM presented by Ankit *et al.* (2013). The results of synkinematic vein sealing revealed how the tracking of the evolving grain boundaries depends on rock wall roughness and opening rate, in agreement with a kinetic theory (Urai *et al.* 1991). Nevertheless, except the surface energy anisotropy defining the crystal shape, no physically related input parameters were chosen, so that a comparison with the real system is not possible.

In the present work, we want to close this gap and adapt a PFM to hydrothermal quartz growth, to describe one of the most important precipitation processes in rock fractures. Whereas previous phase-field approaches to mineral growth relied on a qualitative description of a static crystal shape, in this work we define the combined anisotropy of kinetics and surface free energy, which can capture the observed shape variability of natural crystals. This crystal anisotropy is of special importance for nonfibrous vein growth, where competition between crystals occurs. Because the physical parameters used as input to the model are not all available or are known only to limited accuracy, a hydrothermal experiment is analyzed. Figure 1 presents a flowchart of the strategy applied here: data for interfacial energies and thermodynamics close to the studied pressure, temperature, and composition (p, T, c) of the fluid are selected from the literature. To provide input data for the kinetic anisotropy function, crystal shapes from experimental micrographs are analyzed. This defines the initial model setup, which is then applied for simulations of single crystal and polycrystalline quartz growth. As a subset of the model parameters are still uncertain, these are modified and tested again within small-scale simulations. In a final step, the model is compared to the experimentally obtained morphologies and textures for validation. This is achieved by statistical measures for grain number and orientation distribution as function of the growth distance.

## HYDROTHERMAL EXPERIMENTS FOR QUARTZ VEIN FORMATION

Previous hydrothermal experiments on quartz vein growth by Okamoto *et al.* (2010) and Okamoto & Sekine (2011) are used to extract the missing physical parameters and to give a validation case for the present model. Here, we introduce these experiments briefly. Both experiments were carried out in a pipe-like hydrothermal flow-through reactor with inner diameter of 10.8 mm. Supersaturated solution was produced by dissolution of quartz sand in the first vessel at temperatures of 365°C and fluid pressure of 31 MPa and subsequently precipitation of silica minerals occurred in a second vessel by changing the temperature (Okamoto & Sekine 2011). As the silica solubility in the chosen temperature range is retrograde (Fournier & Potter 1982), the temperature increase to $T = 430$°C in the second vessel
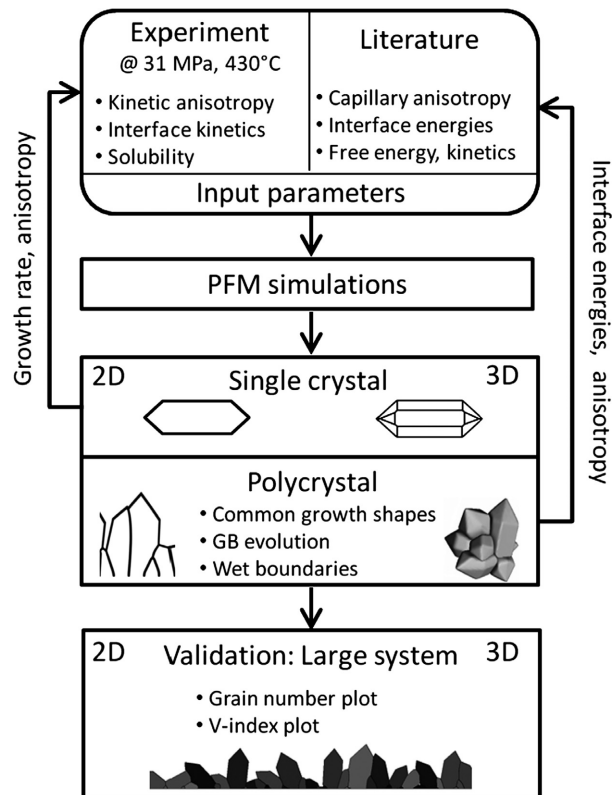


**Fig. 1.** Flowchart of the model adaption process: Available parameters from literature (interfacial energies, quartz kinetics and solubility data) are supplemented with experimental data under the actual conditions (31 MPa, 430°C). Together with the PFM evolution equations, the initial setup is defined, which is tested in restricted scenarios like single crystal or small ensemble growth. Especially anisotropy functions and interface energies are modified within the range of reported values to reveal observed morphologic details. This final model setup is validated in larger simulations reaching the length scale of the experiment.

leads to supersaturation. Previously, dissolution experiments were conducted at $T = 150$–390°C and $p = 31$ MPa to determine the quartz precipitation rate constants used in this study (Okamoto *et al.* 2010). Furthermore, different mechanisms of mineralization were found, depending on the solution chemistry: Pure silica solutions by dissolution of quartz sand gave rise to precipitation of amorphous and microcrystalline polymorphs of quartz. From the solution made by dissolution of granite sand, silica precipitation occurred mainly as epitaxial overgrowth of existing grains (Okamoto *et al.* 2010; Okamoto & Sekine 2011) and was attributed to impurity concentrations of Na, K, and Al in the range of several ppm in the solution.

Small blocks of different quartz-bearing rocks with dimension 5 × 5 × 20 mm were aligned sequentially in the reactor (Okamoto & Sekine 2011). They were cut at the upstream side to create a synthetic 'fracture' of about 300-μm aperture. Flow of the supercritical solution was established by a pressure difference of <0.2 MPa across the precipitation reactor. From the geometry and flow rate of

about 0.017 g sec$^{-1}$, an average initial velocity of about 1.3 mm sec$^{-1}$ can be deduced, indicating vigorous flow. Fluid could pass through the slit as well as along the outer boundaries of the rock blocks; hence, quartz precipitation was observed on either location. As the blocks are immersed in fluid within a circular tube, flow velocity in the slit might have been different and have broken down during sealing. The silica concentrations at the fluid inlet and outlet of the reactor were determined by an inductively coupled plasma atomic emission spectrometer (ICP-AES; Hitachi P-4000). The final crystallized blocks were weighted to determine the average silica concentration at the position of each rock block, using the precipitated mass and the recorded in- and outlet concentrations. 2D thin sections were analyzed under polarized light to determine the *c*-axis direction of the quartz grains by an optical birefringence method.

For the calibration of the growth model in the present study, it is necessary to determine the full orientation, which fixes the cross-sectional shape of the crystals in the prepared samples. To this end, two of the rock samples, listed in Table 1, were characterized again in the present study with respect to grain orientations. With an SEM (Hitachi S3400N), forward-scattering images of thin sections at the outer rock wall were taken with up to 80-fold magnification. Electron backscatter diffraction (EBSD) images taken at selected spots were analyzed automatically to give crystal orientations in form of Euler angle triples (*z*-*x′*-*z″* convention). Several hundred grown crystals at the outer boundary of the rock blocks and grains from the neighboring rock matrix were analyzed. From both optical and EBSD images, it was deduced that all surface-bound crystals are epitaxial overgrowths of rock grains underneath. Figure 2 shows an example of an optical and forward-scattering image from the same location on the outer surface of the metachert sample. In the optical image, the former rock wall can be seen as fine dark line, not visible in the forward-scattering image.

## PHASE-FIELD MODEL

The multiphase-field model used in this work has been discussed and applied to mineral growth previously (Wendler *et al.* 2011; Ankit *et al.* 2013). We briefly introduce the model again so as to (i) motivate two important modifications of the model functions representing crystal anisotropy and kinetic coefficient and to (ii) show how simulation

parameters for an arbitrary growth condition can be generated from thermodynamic and kinetic data. For a more detailed discussion of the model, see Nestler *et al.* (2005), Wendler *et al.* (2011), and Choudhury & Nestler (2012).

### Model equations

Under the constant temperature and volume conditions of the experiment, a local minimization of the Helmholtz free energy $F(\boldsymbol{\phi}, \mathbf{c}, T)$ determines the system's evolution. The independent variables are temperature T, molar concentrations $\mathbf{c} = (c_1, c_i, c_K)$ of $K$ different species and a set of $N$ phase fields $\boldsymbol{\phi} = \{\phi_1(\mathbf{x}, t), \phi_2(\mathbf{x}, t), \ldots \phi_N(\mathbf{x}, t)\}$, which indicate temporally evolving domains with different physical aggregate or order state. Moreover, the phase fields can be seen as volume fraction of the respective phases. In our setup, $N{-}1$ individual crystal grains are represented by $\phi_\alpha$ ($\mathbf{x}, t$) (phase index $\alpha = 1 \ldots N{-}1$), and the liquid phase by $\phi_l$ ($\mathbf{x}, t$) (l = $N$). In the interior or bulk of each phase, $\alpha$ $\phi_\alpha = 1$ holds, which decays continuously to $\phi_\alpha = 0$ in the exterior across the diffuse interface, characterized by the interface width $\varepsilon$. The free energy functional $F$ is formulated as spatial integral of interface and bulk energy density contributions over the simulation domain $\Omega$,

$$F = \int_\Omega \left( \left( \varepsilon a(\boldsymbol{\phi}, \nabla\boldsymbol{\phi}) + \frac{1}{\varepsilon} w(\boldsymbol{\phi}) \right) + f(\boldsymbol{\phi}, \mathbf{c}, \mathbf{T}) \right) \mathrm{d}x. \quad (1)$$

The total interfacial free energy is established by the first two addends in Eq. (1), namely the gradient energy $\varepsilon a(\boldsymbol{\phi}, \nabla\boldsymbol{\phi})$, which energetically penalizes steep changes of $\phi_\alpha$, and the potential $w(\boldsymbol{\phi})/\varepsilon$, which penalizes deviations from the bulk state $\phi_\alpha = 1$ or $\phi_\alpha = 0$. As gradient energy density, we choose here

$$\varepsilon a(\boldsymbol{\phi}, \nabla\boldsymbol{\phi}) = \varepsilon \sum_{\alpha < \beta} \gamma_{\alpha\beta} \left( a_{\alpha\beta}^{cap}(\hat{\boldsymbol{n}}) \right)^2 |\boldsymbol{q}_{\alpha\beta}|^2, \quad (2)$$

where $\boldsymbol{q}_{\alpha\beta} = \phi_\alpha \nabla\phi_\beta - \phi_\beta \nabla\phi_\alpha$ is a generalized gradient vector, pointing in the direction of the interface normal ($\hat{\boldsymbol{n}} = \boldsymbol{q}_{\alpha\beta}/|\boldsymbol{q}_{\alpha\beta}|$), and the subscript $\alpha < \beta$ indicates the summation over all combinations of $\alpha$ and $\beta$. The orientation-dependent interface free energy per unit area is given by $\gamma_{\alpha\beta}(\hat{\boldsymbol{n}}) = \gamma_{\alpha\beta} a_{\alpha\beta}^{cap}(\hat{\boldsymbol{n}})$ (see Garcke *et al.* 1998; Nestler *et al.* 2005 and references therein). The function $a_{\alpha\beta}^{cap}(\hat{\boldsymbol{n}})$ introduces the anisotropy of the interface energy, which is responsible for the evolution of crystal facets in equilibrium. For the second contribution to the interface energy, we chose the multi-obstacle potential, which assumes

**Table 1.** Properties of the two rock samples used for analysis in this study. In addition to the saturation index of the input solution, concentration and saturation indices were determined *a posteriori* using sampled inlet- and outlet concentration and the weighted amount of precipitate along the flow path.

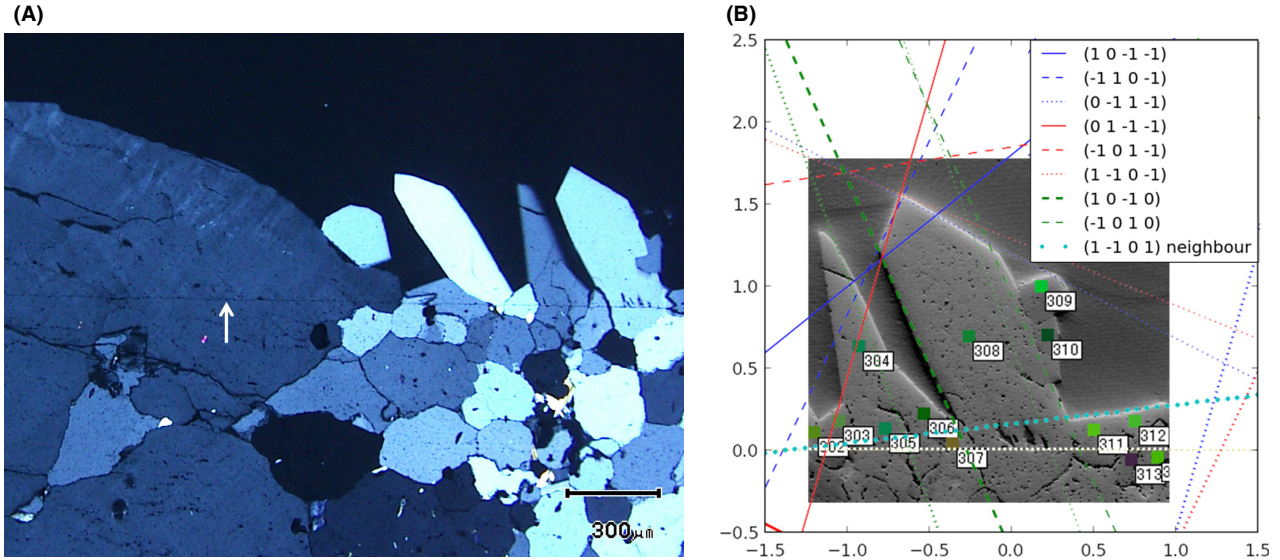| Rock type | Abundance quartz | Grain size (μm) | Saturation input sol. | Si conc. (ppm) | Saturation calc. | growth time (h) | slit width (μm) |
|---|---|---|---|---|---|---|---|
| Metachert | 0.98 | 65 | 3.6 | 115–147 | 1.2–1.5 | 336 | 311 |
| Sandstone | 0.52 | 80 | 3.6 | 127–176 | 1.3–1.8 | 188 | 353 |

**Fig. 2.** Experimental image details. (A) Optical micrograph (polarized light) of outer boundary of the metachert sample. The initial rock wall is still visible as a thin dark line (white arrow, black scale bar is 300 µm) (B) EBSD forward-scattering image of grain 308 and neighbors (rightmost crystal in A). The orientations of all grains at the sample boundary were determined by analysis of the Kikuchi pattern at the locations marked by squares. Intersection lines between ideal crystal facets and the plane of view are plotted after fitting the facet distance relations $d_m/d_z$ and $d_r/d_z$ to determine the crystal shape. Dark patches are multiple small and a few larger fluid inclusions at the initial rock wall (white dotted line in (B)).

$$\frac{1}{\varepsilon} w(\boldsymbol{\phi}) = \frac{1}{\varepsilon}\left( \frac{16}{\pi^2} \sum\nolimits_{\alpha < \beta} \gamma_{\alpha\beta} \phi_\alpha \phi_\beta + \delta \sum\nolimits_{\alpha < \beta < \delta} \phi_\alpha \phi_\beta \phi_\delta \right),$$
(3)

if $\phi_\alpha$, $\phi_\beta$, $\phi_\gamma \in\, ]0, 1[$, and tends to $+\infty$ everywhere else. The third-order term in Eq. (3) with a parameter $\delta \approx 10\gamma_{\alpha\beta}$ is a correction to suppress the formation of spurious third phases $\phi_\delta$ in any $\alpha$–$\beta$ interface (Nestler *et al.* 2005). The last addend in Eq. (1) is the bulk free energy density, which determines the phase equilibria for planar interfaces. It is constructed as interpolation between the free energy densities of the local coexisting phases,

$$f(\boldsymbol{\phi}, \mathbf{c}, T) = \sum\nolimits_\alpha f_\alpha(\mathbf{c}, T)\, h(\phi_\alpha),$$
(4)

with the polynomial $h(\phi) = \phi^2(3\text{–}2\phi)$ as interpolation function. Note that again the index $\alpha$ refers to many 'quartz' phase-fields, the crystal grains, and to one liquid phase field $\phi_l$. The free energy difference between these two phases represents the driving force for crystallization.

The governing equation for the phase fields (Allen–Cahn equation), which provides the local minimization of the free energy Eq. (1), is given by

$$\varepsilon \frac{\partial \phi_\alpha}{\partial t} = \omega(\boldsymbol{\phi}, \nabla\boldsymbol{\phi})\left( -\frac{\delta F}{\delta \phi_\alpha} - \lambda \right) = \omega(\boldsymbol{\phi}, \nabla\boldsymbol{\phi})$$
$$\left( \varepsilon\left( \nabla \cdot \frac{\partial a(\boldsymbol{\phi}, \nabla\boldsymbol{\phi})}{\partial \nabla\phi_\alpha} - \frac{\partial a(\boldsymbol{\phi}, \nabla\boldsymbol{\phi})}{\partial \phi_\alpha} \right) - \frac{1}{\varepsilon}\frac{\partial w(\boldsymbol{\phi})}{\partial \phi_\alpha} - \frac{1}{T}\frac{\partial f}{\partial \phi_\alpha} - \lambda \right).$$
(5)

In Eq. (5), $\delta/\delta\phi_\alpha$ denotes the variational derivative with respect to $\phi_\alpha$, and $(\partial/\partial\nabla\phi_\alpha) = (\partial/(\partial(\partial\phi_\alpha/\partial x_i)))$ is the partial derivative with respect to the components of the gradient vector $\nabla\phi_\alpha$. A Lagrange multiplier $\lambda$ establishes the summation constraint $\sum_{\alpha=1}^{N} \phi_\alpha = 1$. Interfacial kinetics is represented in Eq. (5) by the prefactor $\omega(\boldsymbol{\phi}, \nabla\boldsymbol{\phi})$, defined as interpolation of all local $\alpha$–$\beta$-interface contributions,

$$\omega(\boldsymbol{\phi}, \nabla\boldsymbol{\phi}) = \sum\nolimits_{\alpha < \beta} g_{\alpha\beta}(\boldsymbol{\phi})\omega_{\alpha\beta}(\hat{\boldsymbol{n}}), \text{ with } \omega_{\alpha\beta}(\hat{\boldsymbol{n}}) = \omega_{\alpha\beta}^0\, a_{\alpha\beta}^{\text{kin}}(\hat{\boldsymbol{n}}),$$
(6)

with the interpolation function $g_{\alpha\beta(\boldsymbol{\phi})}$ and a kinetic coefficient $\omega_{\alpha\beta}^0$ for each $\alpha$–$\beta$ interface, that accounts for the difference in attachment kinetics. In addition to the interface energy anisotropy in Eq. (2), the kinetic anisotropy $a_{\alpha\beta}^{\text{kin}}(\hat{\boldsymbol{n}})$ takes into account the orientation dependency of growth rates. Different from former phase-field approaches (Hubert *et al.* 2009; Ankit *et al.* 2013), the kinetic anisotropy is of pivotal importance in this model and will be related to experiments below. For the kinetic coefficients, we restrict to two values $\omega_{\text{sl}}^0$ for the quartz–liquid and $\omega_{\text{ss}}^0$ for the quartz–quartz interfaces (i.e. grain boundaries, GBs). In the current study, the quartz–liquid interfaces are chosen to be very mobile, in contrary to the GBs. In previous applications of this model (Wendler *et al.* 2011; Ankit *et al.* 2013), a simple interpolation of the highly different interface mobilities $\omega_{\text{sl}}^0 \gg \omega_{\text{ss}}^0$ was performed. This averaging creates low values of $\omega$ at the solid–solid–liquid triple junctions, so that it artificially slows down interface motion there. To correctly treat the growth competition between many grains, we propose here a new interpolation function

$$g_{\alpha\beta}(\boldsymbol{\phi}) = \begin{cases} 0 & \text{if } \phi_l > 0 \text{ and } \alpha, \beta \text{ are both solid grains} \\ \dfrac{\phi_\alpha \phi_\beta}{\sum_{\alpha<\beta} \phi_\alpha \phi_\beta}, & \text{else} \end{cases}.$$
(7)

In this way, a constant (high) mobility along all liquid-containing boundaries is maintained, as three-phase regions $\alpha\beta l$ and two-phase boundaries $\alpha l$ ($\alpha$, $\beta$: solid, l: liquid) relax into equilibrium with the same rate.

It should be noted that in general mineralization problems, a diffusion–advection equation for the concentrations and the Navier–Stokes equations for flow must be solved. Below we show why this can be abandoned in the case of quartz growth.

### Input parameters for quartz growth

The task to find appropriate values as input parameters for the PFM is a central part of the modeling process (strategy outlined in Fig. 1). For the mineral $\alpha$-quartz, three different crystal forms are commonly observed (Fig. 3A): (i) six $\{10\bar{1}0\}$ (m) facets of the hexagonal prism capped by two nonequivalent rhombohedral facets, (ii) the positive rhombohedron $\{10\bar{1}1\}$ (z face), and (iii) the negative rhombohedron $\{01\bar{1}1\}$ (r face). The latter is often faster growing as in the example of a natural needle crystal in Fig. 3B, related to a higher impurity uptake (Ihinger & Zink 2000). The atomically rough c face ($\{0001\}$) is the fastest growth direction and does not appear on euhedral crystals. The trigonal crystal system of quartz (point group 32) allows two enantiomorphic left and right handed variants, appearing in equal proportions in nature. We neglect this differentiation here, as the chiral facets $\{2\bar{1}\bar{1}1\}$ and $\{6\bar{1}\bar{5}1\}$ were not observed on the experimentally grown crystals.

### Interface energies

The free energy of the interfaces between quartz and an aqueous liquid is not a unique property. Values between 1.08 J m$^{-2}$ for the fully water coordinated $\{0001\}$ face and 0.12 J m$^{-2}$ for the undercoordinated $\{0001\}$ face have been found by atomistic simulations (de Leeuw

2008). From the analysis of fluid inclusions in a greenschist facies metapelite formed at approximately 300°C and 600 MPa, Hiraga *et al.* (2002) report a value of 0.145 ± 0.055 J m$^{-2}$, which is estimated as quite low due to the effect of high pressure. For this study, we adopt the average values of Parks (1984) under ambient conditions and attribute it to the dominant z face, hence defining $\gamma_{sl} = \gamma_{sl}(z) = 0.360$ J m$^{-2}$ (s and l indicate solid and liquid). All other facet energies are then defined in relation to this energy by calibration of the anisotropy function, thus generating the expected Wulff shape. Due to its influence on the local curvature at the crystal–crystal–liquid junctions, also the grain boundary energy $\gamma_{ss}$ is an important parameter in competitive growth.

For textural equilibrium, the observed dihedral angle $\theta$ indicates the ratio of grain boundary energy and solid–liquid energy and can be calculated from Young's law as $2\cos(\theta/2) = \gamma_{ss}/\gamma_{sl}$. Holness (1993) found a linearly increasing equilibrium dihedral angle for quartz from 60° at 400°C to 80° at 600°C ($p = 400$ MPa). This is supported by Hiraga *et al.* (2002) who reports an angle of 45° for an estimated temperature of 250–300°C. We therefore choose the dihedral angle according to this linear relationship for the temperature of 430°C as 61°, equivalent to a ratio $\gamma_{ss}:\gamma_{sl} = 1.72$.

### Analysis of relative growth rates

The growth shape of a freely growing quartz is determined by the differences in growth rate of its various faces. As no precise data on atomistic growth rates under our experimental conditions are available from literature, we analyzed the shapes of selected needle crystals after the end of the experiment, using thin section images. We assume the crystal shape to preserve the symmetry of the point group; that is, all equivalent faces have the same distance from the ideal crystal center. The crystal center is thought to be located in the middle of the 2D grain area at the surface of the artificial fracture from which epitaxial overgrowth initially starts (the 2D 'seed' area). To reduce the degrees of freedom, we assume that this area is circular. As a consequence, the two relations that determine the final shape
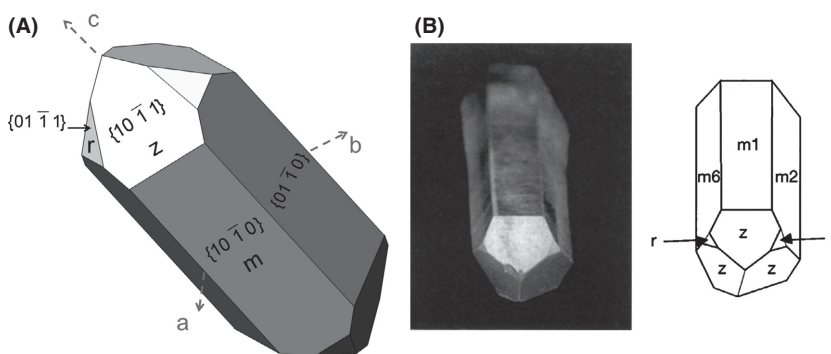


**(A)** **(B)**

**Fig. 3.** Typical growth shape of quartz. (A) z ($\{10\bar{1}1\}$) and r ($\{01\bar{1}1\}$) faces are nonequivalent rhombohedral faces, m ($\{10\bar{1}0\}$, $\{01\bar{1}0\}$) are prism faces (hexagonal unit cell used for indexing). (B) Natural needle shaped Brazilian quartz crystal (diameter $\approx$ 5 mm), which shows dominant slow-growing z faces related to impurity uptake, as analyzed using micro-infrared spectroscopy of growth zone impurities (reprinted with permission from Ihinger & Zink (2000).

are the growth rate of m to z faces, $v_m/v_z$, and that of r to z faces, $v_r/v_z$. As we only choose well-defined euhedral crystals (Fig. 2A, the three larger crystals at the right side), the ratio of growth rates can be approximated by the ratio of distances from the crystal center, for example $v_m/v_z \approx d_m/d_z$. To extract these 3D shape parameters from the 2D thin sections, we apply the following geometrical analysis: we start with an ideal quartz crystal in the reference coordinate frame, its a-axis being parallel to the x coordinate direction, and c-axis parallel to the z-direction. The normal vectors of all facets are calculated in the frame of reference. The distances of the r and m facets ($d_r$ and $d_m$) from the center are predefined to typical values, where z distance is taken as unity, $d_z = 1$. Subsequently, the transformation into the grain reference system is done by rotation using the three Euler angles from the EBSD measurements. The intersection lines between the hypothetical crystal shape and the thin section plane are calculated and plotted as an overlay onto the image (Fig. 2B). In most of the cases, the slopes of the intersection lines unambiguously identify the facet index. A linear scaling is applied to give an optimal match to the width, length, or facet section length. In an iterative procedure, $d_m/d_z$ (the most sensitive parameter), $d_r/d_z$, and the vertical z coordinate of the location of the crystal center are changed, to iteratively improve the fitting. An example for the resulting fit is shown in Fig. 2B for grain no. 308 of the metachert sample. Here, the crystal section is bounded by two z and two m facets with $d_m/d_z = 0.3$ and $d_r/d_z = 1.1$.

To additionally get absolute values for the growth rates, the size of a few selected crystal grains were measured, where the pyramidal tips in c-axis direction were visible in the section plane (sandstone sample, growth duration 311 h). The distance from rock wall to tip was found to be approximately $400 \pm 20$ μm. Using the geometric relationship between c-axis and rhombohedral faces, an absolute average growth velocity of $v_z = 0.03 \pm 0.003$ mm day$^{-1}$ ($3.6 \times 10^{-10}$ m sec$^{-1}$) was calculated.

The average growth rates found by the geometric calibration procedure are given in Table 2 in comparison with previous studies of hydrothermal growth at comparable conditions. Here, all rates from the literature are scaled with the rate of the reference z facet {10$\bar{1}$1}. In addition, for z and c facets, the absolute value in mm day$^{-1}$ is given. The $v_z/v_r$ ratio of about 1:1.1 and the $v_m/v_z$ ratio are quite constant (our ratio of 1:5 is a lower bound), whereas the c/z ratio shows greater changes. On the other hand, when comparing absolute growth rates, the atomically rough c face seems to be to be the proper reference with the smallest variability under pressure and temperature changes. This is mainly due to the lack of a nucleation barrier for this face, whereas growth and dissolution rate of flat faces are determined by the presence and number of screw dislocations. Our growth-rate data compare well to the literature, especially for the industrial quartz growth data from Iwasaki *et al.* (2002). It must be noted that we could not determine the growth rate of the noneuhedral c face experimentally and have chosen a similar factor of $v_c/v_z = 8.6$, giving a total rate of 0.03 mm day$^{-1}$.

## Construction of anisotropy functions

In the approach of the PFM, the crystal growth shape results from a superposition of anisotropy of kinetics an interfacial energy, in accordance with basic crystal growth theory (Sekerka 2005). For vanishing driving force, the interface evolves according to capillary anisotropy $a_{sl}^{cap}(\hat{n})$ only, whereupon the Wulff shape is formed ($\hat{n}$ is the surface normal vector). For larger driving forces, this shape is modulated by the kinetic anisotropy $a_{sl}^{kin}(\hat{n})$ to take into account facet-specific kinetics; hence, the normal velocity varies according to the product of both, $v(\hat{n}) \sim a_{sl}^{cap}(\hat{n}) \cdot a_{sl}^{kin}(\hat{n})$ (see Appendix A). Figure 4(A,B) represents a 2D schematic of this idea where the compact Wulff shape in Fig. 4A is superposed by a kinetic Wulff shape (Fig. 4B) with the same facets, albeit at different distances from the crystal center to give the growth shape

**Table 2.** Growth rates of different quartz forms, as determined from comparable hydrothermal growth experiments or used as input parameters in simulations (last two rows in table). Dimensionless ratios scaled with the rate of the reference z facet ({10$\bar{1}$1}) are listed. Dimensional values for z and c faces in mm day$^{-1}$ are also given.

| r {01$\bar{1}$1} | m {10$\bar{1}$0} | z {10$\bar{1}$1} | (mm day$^{-1}$) | c {0001} | (mm day$^{-1}$) | Reference |
|---|---|---|---|---|---|---|
| 1.67 | 0.0/0.17 | 1 | 0.03 | 8.33 | 0.25 | Iwasaki *et al.* (2002), Table 1* |
| 1 | 0.05 | 0.15† | | 2.87 | 0.43 | Ostapenko & Mitsyuk (2006)‡ |
| 1.03 | – | >1 | 0.007 | 21.5 | 0.16 | Lander *et al.* (2008)§, exp. |
| 1 | 0.16 | 1 | 0.007 | 20 | 0.14 | Lander *et al.* (2008)¶, sim. |
| 1.07 | 0.24 | 1 | 0.03 | <u>8.6</u> | <u>0.26</u> | This work** |

*Grown by industrial process in alkaline Na$_2$CO$_3$/NaOH solution (345°C, 88 MPa). †Exception: in the data from Ostapenko & Mitsyuk (2006), the minor rhombohedral face is taken as reference. ‡Data from Fig. 1 in Ostapenko & Mitsyuk (2006). Grown in hydrothermal reactor (1 M NaOH solution, 360°C, 100 MPa) by dissolution of large c-oriented single crystal due to temperature drop of 10 K at 360°C (relative supersaturation: 2.4–2.8%). §Grown in 0.3 M Na$_2$CO$_3$ solution (69 MPa, 350°C) from single crystalline quartz feed material by temperature drop to 300°C. ¶Adapted to data from Table 2 in Lander *et al.* (2008). **Grown from natural quartz sand ($T = 370$°C, $p = 31$ MPa) by temperature step to $T = 430$°C in Okamoto & Sekine (2011).
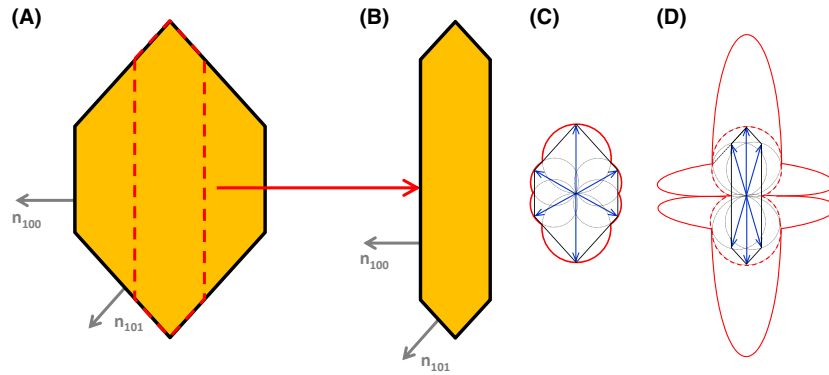
**Fig. 4.** 2D Schematic: Combination of capillary and kinetic anisotropies (only pyramidal and prism facets depicted): For a given equilibrium crystal shape (=Wulff shape) (A), using the functional form Eq. (A2), the capillary anisotropy (C) is defined via the vertex vectors of the polyhedron. To get a growth shape with same growth faces but larger aspect ratio (B), additionally the kinetic anisotropy (D) is defined (in c and d polar plots of the anisotropy functions are given in red, the resulting crystal shape in black and the vertex vectors in blue). In Fig. D, the red solid curve indicates the extended kinetic anisotropy Eq. (A3), which allows for high growth rates in noneuhedral directions (here given as 3:1 for the growth ratio of c to z faces, extension to three dimensions is analogous).

defined above. The equilibrium crystal shape (Wulff shape) is defined here mathematically by a fully facetted interfacial energy anisotropy (Wendler *et al.* 2011; Ankit *et al.* 2013) (Appendix B). The polar plot of the capillary anisotropy function is depicted in Fig. 4C for the two-dimensional case (bold red), constructed as a piecewise composition of circular arcs (spheres in 3D). Due to a lack of reliable facet energies from literature, we evaluated different ratios of the solid–liquid energy of $m$ to $z$ faces (Fig. 1). The choice of $\gamma_{sl}(m) : \gamma_{sl}(z) = a_{sl}^{cap}(m) : a_{sl}^{cap}(z) = 0.786$ results in the depicted aspect ratio of Fig. 4A and resembles closely natural quartz crystals grown close to equilibrium (Suzuki & Kasahara 2010). In the 3D simulations, we assume that both rhombohedral $r$ and $z$ faces have the same interfacial energy.

For the kinetic anisotropy $a_{sl}^{kin}(\hat{\boldsymbol{n}})$, we first choose a different set of vertex vectors (blue) that maintain identical facet directions, but lead to the high aspect ratio shape in Fig 4D (solid black). This shape is implicitly defined by demanding that both capillary and kinetic anisotropy together give the growth ratios found by the calibration procedure (Table 2), for example for the $m$ facet $v(m) \sim a_{sl}^{cap}(m) \cdot a_{sl}^{kin}(m) = 0.786 \cdot 0.3 = 0.24$. The rhombohedral $z$ facet $\{10\bar{1}1\}$ again constitutes the reference, for which we define $a_{sl}^{kin}(z) = a_{sl}^{cap}(z) = 1$. The corresponding polar plot is indicated by the bold red dashed line in Fig. 4D, with the result that the velocity of the vertical prism ($m$) faces are slowed down. Second, we want to prescribe a high value of growth velocity for the $c$-axis (noneuhedral) direction (Lander *et al.* 2008). This leads to a fast development of the crystalline facets. For this purpose, the kinetic anisotropy is modified as detailed in Appendix B (Eq. A3) and given schematically as polar plot in Fig. 4D (bold red). In our setup, we choose a factor of 8.6 for the ratio of $c$- to $z$-direction, close to the hydrothermal growth velocities given by Iwasaki *et al.* (2002).

## Driving force

Whereas the crystalline anisotropies determine relative rates, absolute rates depend on the driving force for crystallization and reaction kinetics, which both need to be defined as functions of the supersaturation. Quartz growth and dissolution can be described by the overall reaction (phase indices s: solid, l: liquid, aq: dissolved)

$$SiO_2(s) + 2H_2O(l) \leftrightarrow H_4SiO_4(aq). \tag{8}$$
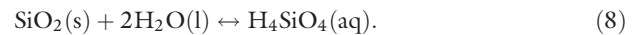
In the context of solution thermodynamics, the driving force of the reaction is given by the free energy difference between crystal and aqueous solution. The change in Gibbs free energy for crystallization of 1 mole of quartz from solution at temperature $T$ is given by (Rimstidt & Barnes 1980; Dove & Han 2007)

$$\Delta G = RT \ln\left(\frac{Q}{K_{sp}(T)}\right) = RT \ln(S), \tag{9}$$

where R is the gas constant, $K_{sp}(T)$ is the temperature-dependent solubility product, and $Q$ is the activity product

$$Q = \frac{a_{H_4SiO_4}}{a_{SiO_2} a_{H_2O}^2} \approx C_{H_4SiO_4}. \tag{10}$$

In the case of low salinity, the activities of water and dissolved silica equal unity, and we can approximate $a_{H_4SiO_4}$ by $C_{H_4SiO_4}$, the molar concentration of orthosilicic acid, and $K_{sp}$ by $C_{H_4SiO_4}^{eq}$, the equilibrium concentration determined for our experimental conditions (98 ppm, Okamoto *et al.* 2010). The driving force is the deviation of the saturation index $S = Q/K_{sp}$ from unity. For a solution concentration of 350 ppm, $S = 3.6$, and the Gibbs free energy difference is 7322 J mol$^{-1}$. In the thermodynamic formulation Eq. (1), Helmholtz free energy densities of liquid and solid phase as function of temperature and chemical composition are necessary. The mechanical work due to the change in molar volume during crystallization at 31 MPa equals

$p\Delta V = p\left(V_m^{\mathrm{Qtz}} - V_m^{\mathrm{H_4SiO_4(aq)}}\right) \approx 145 \ \mathrm{J \ mol^{-1}}$ and can therefore be neglected. Hence, we may approximate the Helmholtz free energy $F = G{-}pV$ with the Gibbs free energy.

To convert Eq. (9) into a free energy density, it has to be divided by the molar volume of quartz, $V_m^{\mathrm{Qtz}}$. One has to bear in mind that one unit volume of solution includes solute of a much smaller volume of quartz when precipitated. For a dilute solution, this fraction is given by the difference of actual and equilibrium silica concentration, multiplied with the ratio of dissolved silica molecular volume to water molecular volume. Although water is in a supercritical state at our experimental conditions, we assume the volume fraction of silica and water to be well approximated by $V_m^{\mathrm{Qtz}}/V_m^{\mathrm{H_2O}}$ at low temperatures. Thus, the free energy density difference is

$$\Delta f(C_{\mathrm{H_4SiO_4}}) = \left(C_{\mathrm{H_4SiO_4}} - C_{\mathrm{H_4SiO_4}}^{\mathrm{eq}}\right) \frac{v_m^{\mathrm{Qtz}}}{v_m^{\mathrm{H_2O}}} \cdot \frac{RT}{v_m^{\mathrm{Qtz}}} \ln\left(\frac{C_{\mathrm{H_4SiO_4}}}{C_{\mathrm{H_4SiO_4}}^{\mathrm{eq}}}\right)$$
$$= C_{\mathrm{H_4SiO_4}}^{\mathrm{eq}} \frac{RT}{v_m^{\mathrm{H_2O}}}(S-1)\ln(S),$$
(11)

giving $\Delta f = 1.059 \times 10^5 \ \mathrm{J \ m^{-3}}$. In the bulk free energy formulation Eq. (4), we assign to each solid phase (representing a crystal grain) a free energy of $f_s = 0$ and to the aqueous solution the value from Eq. (11), $f_l = \Delta f$. The difference establishes the driving force for crystallization, $\Delta f = f_s{-}f_l$, which is assumed to be constant according to a constant supersaturation at all quartz interfaces. This implies that diffusion and advection are neglected and the growth rate of the grains is assumed to be completely dominated by interface kinetics. This assumption is admissible if: (i) the rate of advection at the crystal interface is large compared to the rate of diffusion, (ii) the average flow velocity is large compared to the growth rate of the crystal, and (iii) the flow is mostly laminar and uniform, ensuring a constant gradient at the thin concentration boundary layer adjoining the crystal–liquid border. If we set the characteristic length scale in the flow problem to the fracture aperture of 300 μm and the estimated average velocity of 1 mm sec$^{-1}$ and take density and viscosity of water at the given supercritical conditions (IAPWS 2007), the calculated Reynolds number of Re = 1.8 indicates that the final condition is met. The first two conditions can be evaluated by calculation of the dimensionless Peclet number Pe and Damköhler number of second kind Da$_{\mathrm{II}}$, (see e.g. Dijk & Berkowitz 1998). Pe is defined as quotient of advective versus diffusive transport rate, and Da$_{\mathrm{II}}$ as ratio of reaction rate to diffusion rate. With the diffusivity of silica in supercritical water at our growth conditions of $5 \times 10^{-8} \ \mathrm{m^2 \ sec^{-1}}$ (Walton 1960), Pe = 7 follows, and taking the average quartz growth velocity of $v = 3.5 \times 10^{-10} \ \mathrm{m \ sec^{-1}}$, Da$_{\mathrm{II}}$ = 3 × 10$^{-4}$. Hence, under

the actual experimental conditions, diffusion is fast compared with crystal growth. It was previously demonstrated that the crystallization process is dominated by interface kinetics and not solute transport (Okamoto et al. 2010). According to the Peclet number, advection and diffusion are nearly of the same order, so that no concentration-depleted crystal–liquid boundary layers are to be expected in laminar flow. A similar argument was given for a simulation study of quartz growth by Lander et al. (2008). Nevertheless, the estimations given here will break down in the late stage of crack sealing, because the characteristic length scale then reduces to typical pore sizes.

Interface kinetics

For a supersaturation of the inlet fluid of $S = 3.6$, the experimental growth velocity was evaluated to be 0.03 mm day$^{-1}$. For general situations, the value of the kinetic coefficient ω in the phase-field Eq. (5) as function of supersaturation and temperature must be given. Assuming that the growth-rate $r_{\mathrm{gr}}$ of the quartz–solution interface depends linearly on the saturation index, transition state theory gives

$$r_{\mathrm{gr}} = k_-\left(\frac{Q}{K_{\mathrm{sp}}(T)} - 1\right) \approx k_-\left(\frac{C_{\mathrm{H_4SiO_4}}}{C_{\mathrm{H_4SiO_4}}^{\mathrm{eq}}} - 1\right) = k_-(S-1),$$
(12)

where $k_-$ is the precipitation rate coefficient (Rimstidt & Barnes 1980) for a system containing 1 kg of solute and 1 m$^2$ of quartz surface area. From Eq. (12), we get an equivalent interface velocity by multiplication with the quartz molar volume and division by the ratio of surface area and solute mass as

$$v_{\mathrm{gr}} = \frac{V_m^{\mathrm{Qt'z}} r_{\mathrm{gr}}}{A_s/M} = V_m^{\mathrm{Qtz}} \hat{k}_-(S-1).$$
(13)

(Rimstidt & Barnes 1980), where $\hat{k}_-$ is now the rate coefficient with units in mol m$^{-2}$ sec$^{-1}$. Dissolution–precipitation series in the temperature and pressure range of our experimental setup were carried out in (Okamoto et al. 2010), from which the rate coefficient was determined as $\log(k_-) = -0.0886 - 2638/T \ \mathrm{s^{-1}}$ ($T$ in $K$) and the surface-to-mass ratio $A_s/M = 33.6 \ \mathrm{kg \ m^{-2}}$ for $T = 390°C$.

At higher supersaturation, when curvature effects can be neglected, the growth velocity in the PFM scales for a solid–liquid boundary as $v = \omega_{\mathrm{sl}}^0 \Delta f$ (Appendix A). With Eq. (13) and the free energy difference Eq. (11), the model kinetic coefficient can now be defined as

$$\omega_{\mathrm{sl}}^0 = \frac{v_{\mathrm{gr}}}{\Delta f} = \frac{v_m^{\mathrm{Qtz}} v_m^{\mathrm{H_2O}} k_-}{C_{\mathrm{H_4SiO_4}}^{\mathrm{eq}}(A/M)RT\ln(S)}.$$
(14)

With the values of molar data given in Table 5, the kinetic coefficient amounts $\omega_{\mathrm{sl}}^0 = 2.39 \times 10^{-15} \ \mathrm{m^4 \ Js^{-1}}$. In the derivation of Eq. (14), a value of $S$ substantially larger than 1

has been imposed. The kinetic coefficient for grain boundary motion $\omega_{ss}^0$ is chosen two orders of magnitude smaller to avoid substantial grain boundary migration within the simulation time. It must be noted that grain boundary motion is an important process for longer time scales in the evolution of metamorphic rocks and has been simulated with this model for the case of partial melts in Wendler *et al.* (2009).

Parameter set

For the simulations, each model parameter with physical units is nondimensionalized by dividing it by the respective scale quantity and listed in column 5 of Tables 3–5. From a simple dimensional analysis of the phase-field equation Eq. (5), the scales for energy density $f_0$, surface tension $\gamma_0$, length $l_0$, time $t_0$ and kinetic coefficient $\omega_0$ are related as $f_0 = \gamma_0 / l_0$ and $t_0 = l_0^2 / \omega_0 \gamma_0$ (Wendler *et al.* 2009). Hence, choosing a scale for length and interface tension determines the energy scale (an inaccurately chosen interface tension will change the driving force), and choosing a scale for the kinetic coefficient gives the time scale, provided that length and interface energy are fixed. Here, we set $l_0 = \Delta x = 1$ μm as the distance between two grid points to well resolve the smallest grains, $\gamma_0 = 0.36$ J m$^{-2}$ as the solid–liquid interface tension of quartz and the above-defined kinetic coefficient as $\omega_0 = 2.39 \times 10^{-15}$ m$^4$ Js$^{-1}$. From this, an energy density scale of $f_0 = 3.6 \times 10^5$ J m$^{-3}$ and a time scale of $t_0 = 1162$ sec follow.

## RESULTS AND DISCUSSION

We now apply the PFM for quartz growth starting from single nuclei and polycrystalline seeds mimicking the rock

wall. In all simulations, we use the parameters from Tables 3–5 with one exception: According to the parameter adaption procedure given in Fig. 1, supersaturation indices $S$ in the range of the experimentally determined values (Table 1) are varied to account for observed differences between simulation results and experiment. The respective driving forces and kinetic coefficients are then calculated according to Eqs (11) and (14). For vein growth, the three dimensionality of the processes is essential, as morphogenesis by growth competition involves fast-growing directions on the whole orientation space of the crystal. Nonetheless, as a computationally faster approach to test various parameter configurations, we also applied 2D simulations. The phase-field Eqs (5) are solved here using combined finite difference and finite volume techniques on a regular grid, with an explicit time update and a second-order accurate spatial discretization. Computation time is reduced by parallelization and algorithmic optimization (Nestler *et al.* 2008b), so that the simulations presented in this work could be solved on a quadruple core desktop PC.

## Single crystal

The simplest test of the model is the shape evolution of a single crystal in 2D. Growth started from a circular seed of 60 μm diameter according to the typical grain size and a driving force of $\Delta \tilde{f} = 0.15$ was applied, corresponding to a supersaturation of $S = 2.7$. The growth velocity was determined from the phase-field locations $\phi_s = 0.5$ along facet normals. The velocity of the $z$ (inclined) and $m$ (vertical) facets and of the $c$-direction (long axis of crystal) is plotted versus logarithmic time in Fig. 5A, with the solid phase-field depicted at different time steps as insets. During the development of the facets, the velocities asymptotically converge to the theoretically predicted values given by $v(t\hat{n}) = \tilde{\omega}_{sl}^0 a_{sl}^{kin}(\hat{n}) a_{sl}^{cap}(\hat{n}) \Delta \tilde{f}$ (Appendix A), which here is $v(z) = 0.15$ and $v(m) = 0.035$. When the faceting is complete, the $c$-axis velocity drops quickly by a factor of about 9 (given by the selected kinetic anisotropy). This dynamical change results in an initial velocity advantage for the

**Table 3** Numerical and model parameters.

| Numerical parameter | Symbol | Eq. | dim. value | dim.less value |
|---|---|---|---|---|
| Grid spacing | $\Delta x$ | – | 1 μm | 1.0 |
| Time stepwidth | $\Delta t$ | – | 58 sec | 0.05 |
| Interface width | $\varepsilon$ | 1, 2, 3 | 4 μm | 4.0 |
| Higher order potential parameter | $\delta$ | 3 | 4.32 J m$^{-2}$ | 12.0 |

**Table 4** Interfacial parameters (s: solid, l: liquid).

| Interfacial parameter | Symbol | Eq. | Dim. value | Dim. less value | Reference |
|---|---|---|---|---|---|
| s–l interface tension (z face) | $\gamma_{sl}(z)$ | 2, 3 | 0.36 J m$^{-2}$ | 1.0 | Parks (1984) |
| Interface energy anisotropy function | $a_{\alpha\beta}^{cap}(\hat{n})$ | 2 | Defined by Wulff shape: $\gamma_{sl}(r){:}\gamma_{sl}(z)$: $\gamma_{sl}(m) = 1{:}1{:}0.786$ | | This work |
| s–s interface tension | $\gamma_{ss}$ | 2, 3 | 0.62 J m$^{-2}$ | 1.72 | Hiraga *et al.* (2002); Holness (1993) |
| s–l kinetic coefficient (z face) | $\omega_{sl}^0(z)$ | 6 | $2.39 \times 10^{-15}$ m$^4$ J$^{-1}$ s$^{-1}$ | 1.0 | Exp., this work |
| Kinetic coefficient anisotropy function | $a_{\alpha\beta}^{kin}(\hat{n})$ | 6 | defined by kinetic Wulff shape: $v_r{:}v_z$: $v_m = 1{:}1.07{:}0.3$ | | This work |
| s–s kinetic coefficient | $\omega_{ss}^0$ | 6 | $2.39 \times 10^{-17}$ m$^4$ J$^{-1}$ s$^{-1}$ | 0.01 | |

**Table 5** Bulk parameters. Physical parameters (for $S = 3.6$) are given without non-dimensional values, as they only enter the calculation of the free energies (scale parameters are given in the text).

| Bulk parameters | Symbol | Eq. | Dim. value | Dim. less value | |
|---|---|---|---|---|---|
| Free energy, liquid | $f_l$ | 4 | 0 | 0 | Calculated, this work |
| Free energy, crystal | $f_s$ | 4 | $1.059 \times 10^5$ J m$^{-3}$ | 0.294 | Calculated, this work |
| Temperature | $T$ | 1, 2, 11, 14 | 703 K | | Okamoto & Sekine (2011) |
| H$_4$SiO$_4$ equil. conc. | $C^{eq}_{H_4SiO_4}$ | 11, 14 | $98 \times 10^{-6}$ | | Okamoto & Sekine (2011) |
| H$_4$SiO$_4$ concentration | $C_{H_4SiO_4}$ | 11, 14 | $350 \times 10^{-6}$ | | Okamoto & Sekine (2011) |
| Rate coefficient for quartz precipitation | $k_-(T)$ | 14 | $k_- = -0.0886$ to 2638/T s$^{-1}$ | | Okamoto *et al.* (2010) |
| Ratio quartz surface area versus mass | $A_s/M$ | 14 | 33.6 m$^2$ kg$^{-1}$ | | Okamoto *et al.* (2010) |

**(A)**                             **(B)**    **(C)**



**Fig. 5.** (A) Facet velocities from a 2D simulation of single crystal growth from a circular nuclei of 60 μm diameter (grid size: 600 × 600). The velocities along the $z$ and $m$ facets approach the theoretical values (dotted line), and along the noneuhedral $c$-axis, a velocity transition after full development of facets is observed. Phase-field profiles are displayed as insets at four time steps (indicated by arrows). (B) A crystal grown from a 40 μm seed reaches its $c$–$m$ aspect ratio of 8.2 predicted by the model at a growth distance of about 1200 μm. (C) At vanishing driving force, the crystal shape changes to the equilibrium shape (ECS) given by the interface energy anisotropy.
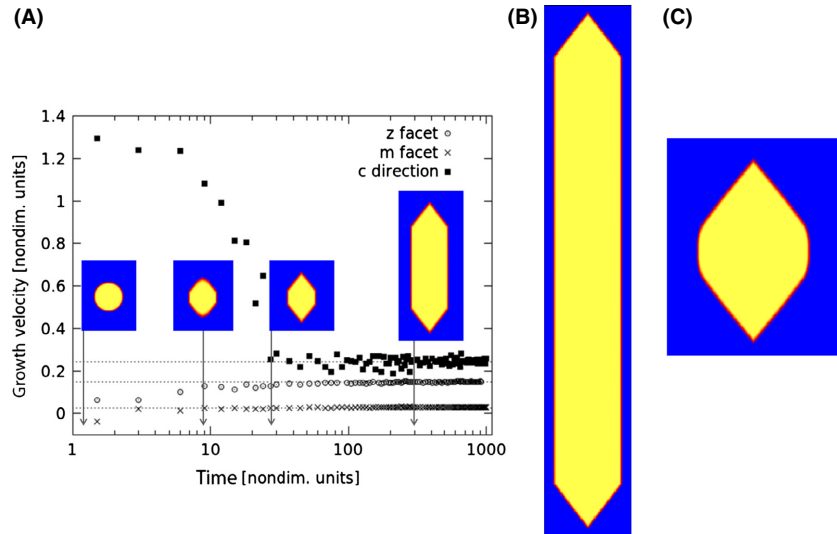
noneuhedral orientations. Thus, larger fracture openings will privilege growth of noneuhedrally terminated grains during the crack-sealing process, followed by competitive growth for crystals with well-developed facets (Urai *et al.* 1991). The crystal finally achieves a constant shape ratio of $d_m{:}d_z = 0.21{:}1$ after a duration $t = 8.8$ days (physical time, $t_0 = 904$ s) having a long axis of 0.5 mm (Fig 5B). To simulate solid–liquid equilibrium conditions, we use a method which adjusts the actual driving force in each time step as to conserve the initial volume of the crystal (Nestler *et al.* 2008a). Starting from a circular crystal of 200 μm diameter, the shape in Fig. 5C finally develops. This is close to the geometry we used as input for the capillary anisotropy (Fig 4A) and confirms that evolution is now dominated by interface energy minimization.

The evolution of a 3D quartz crystal was also simulated with the anisotropy combination according to the calibration procedure described above. In this case, a spherical nuclei of 40 μm diameter at a supersaturation of $S = 3.9$ grew within a physical period of 6.1 days to a size of 0.5 mm (Fig. 6A). The growth rates in 2D and 3D of 0.05–0.08 mm day$^{-1}$ compare well to the estimated experimental value of 0.03 mm day$^{-1}$. Crystal facets of the same crystal zone with different growth rates will change their relative size in time. This may lead to the complete

elimination of the faster growing facet (Iwasaki & Iwasaki 1995). In the simulations, this can be observed as a slow decay of the minor rhombohedral $r$ faces, for which we have set a slightly higher growth rate $v_r/v_z = 1.1$ in relation to the $z$ faces, see Fig. 6A (right image). This change in relative size of $z$ versus $r$ faces in time has also been found in natural quartz crystals by analysis of growth sectors (Ihinger & Zink 2000). In Fig. 6B, the initial stage of the same process is shown, where a spherical nucleus has been set. The crystal has relaxed into the 3D Wulff shape with its compact habit and now starts to grow predominantly along the $c$-axis direction, which was rotated here for 55° versus the $y$-axis.

## Polycrystal

After ensuring that the habits and growth rates of simulated and real single crystals coincide well, we studied polycrystalline growth with a focus on morphological details. In this case, the triple junction (quadruple junction in 3D) dynamics become important. The dynamics are influenced by the magnitude of the grain boundary energy, but this parameter is not well determined and deviations from the reference value in Table 4 were also tested (see the procedure given in Fig. 1).
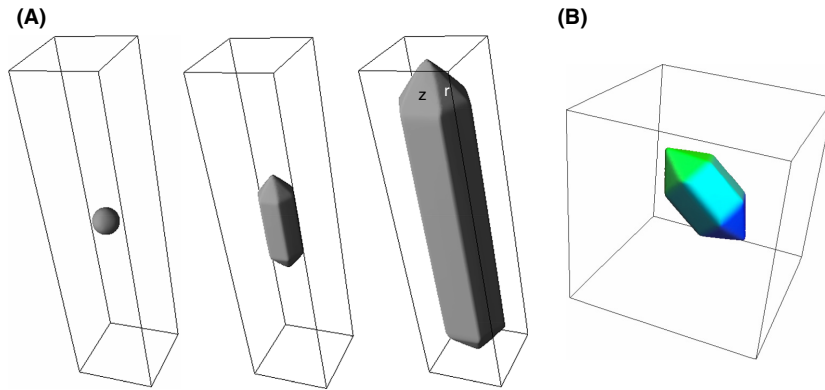
**Fig. 6.** (A) Evolution of a 3D single crystal into its growth shape (grid size: 120 × 120 × 500). As the growth ratio of *z* to *r* faces was defined as $v_r/v_z = 1.1$, the major rhombohedral faces (*z*) gradually grow larger, while the minor *r* faces decrease. (B) In the initial stage, a spherical nucleus relaxes into its equilibrium shape, before elongated growth along *c*-axis sets in (color indicates spatial orientation).

In a 2D scenario, equally sized crystals with random orientation were placed adjacent to form flat films of constant height, as to reproduce the respective rock surface prepared by a micro-cutter in the experiment. Periodic boundary conditions were applied along the *x*-direction, that is a horizontal wrapping of the simulation box. First, simulations were repeated at least 20 times with the standard model setup (Table 3–5) always using different grain orientations. Figure 7 (A–C) shows that, after an initial competition process, quartz crystals with *c*-axes subnormal to the substrate prevail. The widening crystal bases closely resemble the sectional images of the samples (e.g. Fig. 7E). Grain boundaries between the larger crystals are chiefly straight. The grain boundary directions can be well explained by the propagation of the adjoining facets in normal direction according to their velocity, as proposed previously by Urai *et al.* (1991). Sudden directional changes appear, when one of the triple junction facets gets consumed and is replaced by another one of the same crystal. Especially at small grain size, curved boundaries evolve in competitive growth, where capillary forces must have rotated the triple junction. As an example, a detail from a forward-scattering image (metachert sample) with similar features is included in Fig. 7E, where the *c*-axis orientations of the neighboring crystals projected to the plane of view are comparable to the 2D simulation. The fast kinetics we have defined for the c-axis orientation causes a nearly instantaneous formation of pyramidal crystal tips for those grains aligned subnormal to the rock wall (Fig. 7A). These have clearly an initial advantage over the stronger misaligned ones, which form facets without propagating much into the liquid. This effect becomes more pronounced with increasing size of the seed grain and is probably responsible for several exceedingly large crystals found in the quartz thin sections, which protrude further into the solution space than the well-aligned crystals (see Fig. 2A, leftmost crystal).

Another noticeable feature commonly found both in 2D and 3D simulations and sample images are 'bicrystals' composed of two grains with slightly differing *c*-axis orientations that adopt a common convex shape during growth (e.g. Fig. 7B and E, left sides). The liquid phase-field profile of the final stage is given in Fig. 7F. Obviously, a small amount of liquid phase is incorporated into the grain boundary during propagation of the bicrystal triple junction. From analysis of simulations with different orientation, we conclude that this partially wet film predominantly appears between grain pairs with similar *c*-axis orientation. Hence, the wet boundaries track approximately the direction of the quartz prism (*m*) faces, and furthermore remains stable only if supersaturations are chosen lower than $S = 3.0$. The existence of a stable liquid film at a small driving force is not an artifact of the model. It follows from the value of the grain boundary energy relative to that of the solid–liquid free energy of an m face that a total wetting condition is fulfilled ($2\ \tilde{\gamma}_{sl}(m) = 1.57 < \tilde{\gamma}_{ss} = 1.72$, Table 4). In the sample images, grain boundaries with trails of fluid inclusions are frequently found (example indicated by an arrow in Fig. 7E), which may be a remainder of a wet boundary. Also, sometimes larger fluid inclusions appear as worm-like features (at the base of the rightmost crystal in Fig. 2B).

Capillary and kinetic anisotropy were defined in the model using different shapes. This leads to a dependence of the evolution of quartz equilibrium and growth shapes on driving force. To test whether we can remove this degree of freedom, both anisotropies were configured with the same Wulff shape in a second simulation setup. A final time frame is shown in Fig 7D. Again, growth competition occurs, but a more contiguous quartz surface develops, significantly different from the micrographs.

To verify the measured orientation parameters (Euler angles) and to perform a direct comparison with the experiment, ensembles of four to eight quartz grains were selected from the sample micrographs and 3D simulations were carried out. From micrographs and EBSD measurements, the width of the grains at the former rock wall boundary and their orientation was determined. Using this as input, a starting scenario as depicted in Fig. 8A was created. The initial seed shapes were chosen as ellipsoids with the grain width as major axis, and the center position

**Fig. 7.** 2D quartz growth from rock wall with 10 equisized seeds (color scale for *c*-axis angle given in A, grid size: 350 × 400, supersaturation *S* = 2.35, same initial configuration). (A–C) Time sequence showing quartz needle evolution, using the combined anisotropy developed for the experimental conditions. (D) Compact quartz surface results when applying the same anisotropy function for surface energy also for kinetics. In both cases, crystals aligned normal to the fracture surface (orange to red) prevail, and 'bicrystal' shape develops. (E) Sample detail with *c*-axis orientations of grains comparable to simulation and adapted to the same length scale. (F) Liquid phase-field showing partially wet grain boundaries for specific orientations (red stripes, indicated by arrow).
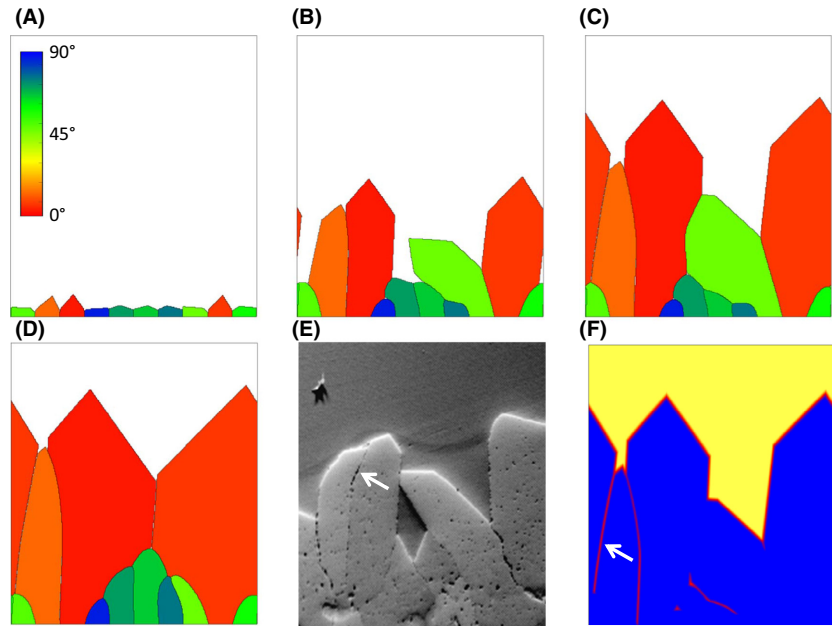
approximated by performing the shape fitting procedure as described above. The ellipsoidal shaped sample grains were embedded in a tiling composed of grains with *c*-axis sub-parallel to the rock wall, to account for neighbors in the third dimension (Fig. 8A). For this specific configuration, the central subnormally aligned grain no. 236 had a left and right neighbor (241 and 242) with identical orientation, and it is hence treated as a single grain (Fig. 8E). Figure 8 (A–C) shows the evolution of one specific microgeometry over the physical time of 8 days, with the final structure intersected at the expected position (Fig. 8A, white dashed line) in Fig. 8D. An additional grain growing into the field of view externally from outside of the section (sample image in Fig. 8E, no. 237) was not taken into account. The unknown details of the initial geometry introduce a source of error in the simulations. Nevertheless, a good agreement is found, especially when comparing absolute size of grains and orientation of facet intersections (central grain no. 236 in Fig. 8D).

### Validation: large system

As a final step, the hydrothermal growth of quartz on a length scale comparable to the size of the synthetic fracture aperture (~300 μm) was studied. In contrast to the micro-ensemble simulations, random configurations of grains sizes and orientations were applied, and averaged properties describing evolution of grain number, texture, and sealing time analyzed. The simulation grid size was adapted to match the physical size of the experiment and the number of grains chosen so that the average grain size of the rock samples (Table 1) was reproduced.

In Fig. 9A, the final stage of the experiment after 311 h is shown for free growth at the outer rock wall of the metachert sample. Mostly crystals with *c*-axis orientation subnormal to the wall rock advance, and those inclined for more than 45° are completely replaced. For the 2D simulation under corresponding growth conditions, 50 grains with random orientations in the range of −90° to +90° and average grain size of 65 μm were used. Fig. 9B shows the simulation after a physical time of 200 hours when the largest quartz crystals reached the same size as in the micrograph (Fig. 9A) of 350 μm. Both experiment and simulation show the evolution of a crystallographically preferred orientation (CPO) as the orange-to-red-colored grains prevail, with their fast-growing *c*-axis oriented subnormal to the wall (note the difference in color scaling from 0 to 45° for experiment and simulation). An unexpected effect is the dependence of crystal fabric on the supersaturation (or driving force): The same setup with saturation index reduced from 3.6 to 1.8 results in the microstructure given in Fig. 9C, where the competition sets in much faster and leaves only the well-aligned crystals growing in isolation. When decreasing the supersaturation further down to values of $S \approx 1.8$, growth cedes for most seeds, with the exception of few grains which finally occupy the whole liquid space. The reason for this behavior is a predominance of capillary forces in this low supersaturation regime: Crystal tips as well as grain–grain–liquid junctions produce interface curvature, which constitutes a negative driving force preventing growth or even inducing dissolution of specifically oriented grains.

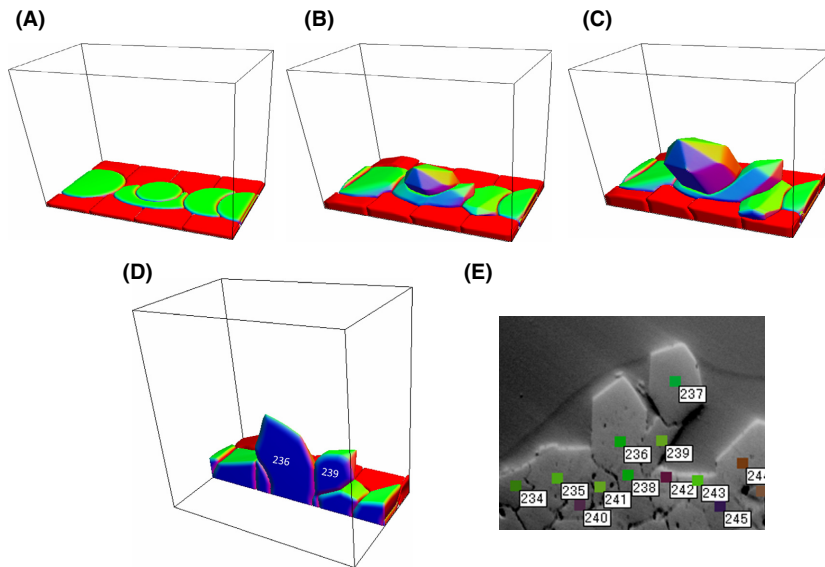Accordingly, 3D simulations of free polycrystal growth were carried out using an initial setup of 150 randomly

**Fig. 8.** Test of the 3D phase-field model in a micro-setup, with grain size and full orientation determined from EBSD measurements (laterally periodic boundaries, grid size: $150 \times \times 90 \times \times 150$, color represents surface orientation). (A–C) Three time steps showing the evolution of 5 grains (no. 235, 236, 239, 241 = 242, 243 from Fig. 8(E) in perspective view. Central prismatic grain is no. 236. (D) Final stage with grain structure shown as intersection. (E) Forward-scattering image showing the grain ensemble and numbering. Rock wall position is indicated as gray dashed line.
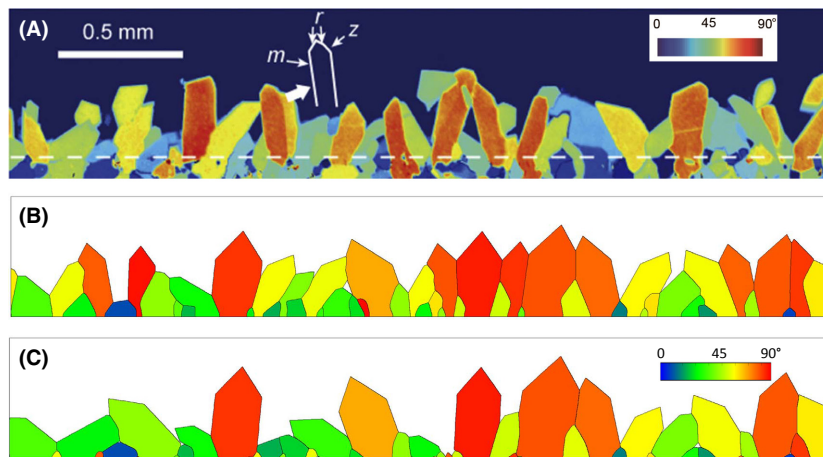


**Fig. 9.** Experiment and simulation images of free growth, scaled to the same physical size. (A) *c*-axis orientations from outer rock boundary for the metachert sample, determined by birefringence measurements (average grain size 23 μm). The color scaling is similar to the simulations (red: *c*-axis perpendicular, blue: parallel to rock wall). (B) 2D simulation with identical grain size and random orientation (grid size: $3200 \times 465$). (C) Setup as in B, but under supersaturation $S = 1.8$ (Image A reproduced from Fig. 4B in Okamoto & Sekine (2011), reprinted with permission).

oriented grains at the bottom of a simulation box of $600 \times 600 \times 540$ μm size, for which we used doubled grid spacing $\Delta x = 2$ μm to lower computational costs. The initial grains were randomly distributed in a flat seed layer by a 2D Voronoi tessellation algorithm, thereby ensuring that the average grain size corresponds to the rock wall grain size. As it is increasingly complicated to compare 3D random microstructures to 2D micrographs, we use the statistical measures as proposed by Okamoto & Sekine (2011): First, the number of grains plotted as function of increasing distance to the rock wall quantifies the speed of the growth competition process (development rate of a CPO). Distance $L$ will always be scaled in the following with the average grain size $d$, which was found to be the relevant length scale in growth competition (Okamoto & Sekine 2011). For the two samples in our study (metachert and sandstone), the experimentally determined grain num-

ber scaled with the number of grains in the initial rock wall layer is plotted versus the scaled distance $L/d$ in Fig. 10A (open and closed squares). The largest crystals had grown up to a distance of $L/d = 6$, about 400 μm. Negative values of distance indicate positions in the original rock. From the simulation frames we chose those for analysis where the largest crystals had grown the same distance of 400 μm. The grain evolution for the standard parameter set in 2D (red line) and 3D (small red circles) both fit very well to the experimental value. To get comparable results, it was important to exactly follow the experimental procedure, which was done with 2D thin sections. Accordingly, we used 2D slices of the 3D simulation data parallel to the growth direction and counted grain numbers (and orientations) scanning line after line perpendicular to growth.

The *c*-axis orientation of the rock samples is not completely random (Fig. 11B at the rock wall). Hence, a 2D
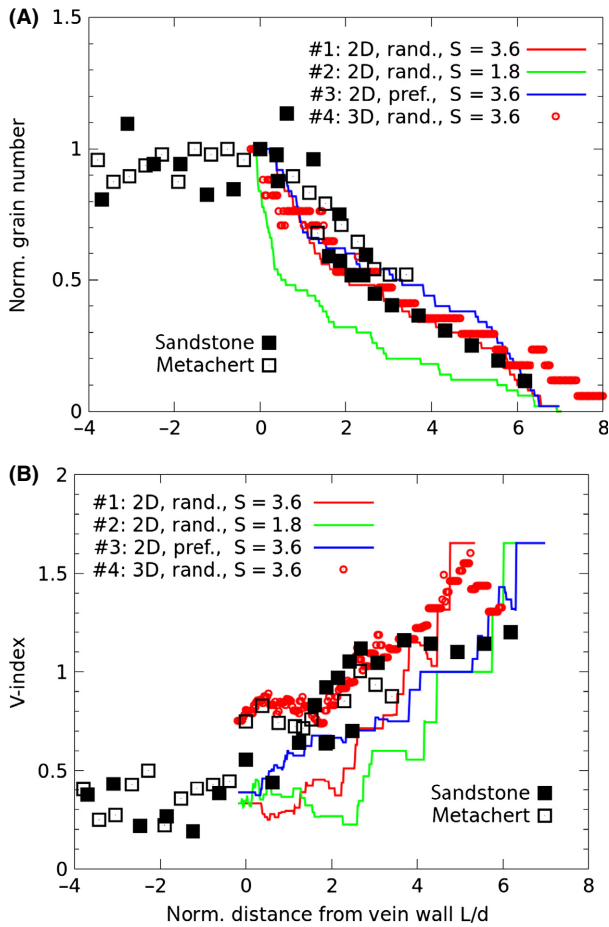
**Fig. 10.** Statistical comparison of experiment and simulations (solid lines for 2D and small circles for 3D) for competitive free growth. Sample data are given by filled and open black squares. Simulations #1–#3 are in 2D, #4 in 3D. Supersaturations are $S = 3.6$, except simulation #2 ($S = 1.8$). All simulations start with random grain orientations, except simulation #3, where a preferentially subnormal c-orientation distribution was created. (A) Number of surviving crystals, normalized with number of grains at the initial vein/host rock boundary. (B) c-axis fabric measure (V-index) quantifying deviation from random c-axis orientation distribution.

simulation was started with a preferential orientation distribution normal to the rock wall to match the preexisting texture, which gives a similarly good agreement (#3 in Fig. 10A, blue line). In contrast, a simulation with low supersaturation $S = 1.8$ (#2, resulting in the microstructure of Fig. 9C), indicated by the green line, clearly deviates from the experimental data. The stronger decay of the grain number plot indicates a fast initial selection process.

In addition, deviation of the observed orientation distribution $R_{obs}(\theta)$ of an analyzed set of grains from a random orientation distribution $R_{rnd}(\theta)$ can be determined by calculating the V-index (Okamoto & Sekine 2011):

$$V = \int_0^{\pi/2} |R_{rnd}(\theta) - R_{obs}(\theta)|d\theta \approx \sum_i^n |R_{rnd}(\theta) - R_{obs}(\theta)|\Delta\theta$$

$$\text{with } \Delta\theta = \frac{\pi}{2n} \text{ and } R_{rnd}(\theta) = \cos\left(\frac{\pi}{2} - \theta\right) - \cos\left(\frac{\pi}{2} - (\theta + \Delta\theta)\right)$$

(15)

The integral in this calculation extends over the possible angles between the c-axis orientation and the fracture normal $\theta$ from 0 to 90° and is approximated in Eq. (15) by a discrete summation of $n$ (here $n = 9$) bins of angular width $\Delta\theta$. Thus, a V-index of 0 indicates complete random fabric, whereas the maximum of 1.67 (for $n = 9$) is reached for perfect alignment of all grain c-axes. Grain orientations have been analyzed along lines perpendicular to the fracture boundary in a thin section (as in 2D simulation images, for 3D simulation layer, slices were used in the same way). The V-index plotted again as function of scaled distance $L/d$ from the seed plane is depicted in Fig. 10B for both rock samples and the 2D and 3D simulation discussed above. The 2D simulation results (#1, #2) obviously deviate in magnitude from the experiment, but show the same general trend. The metachert sample shows a step-like increase at the rock wall, which could be attributed to a selective growth of grains with subnormal c-axis orientations. To test this hypothesis, we modified the
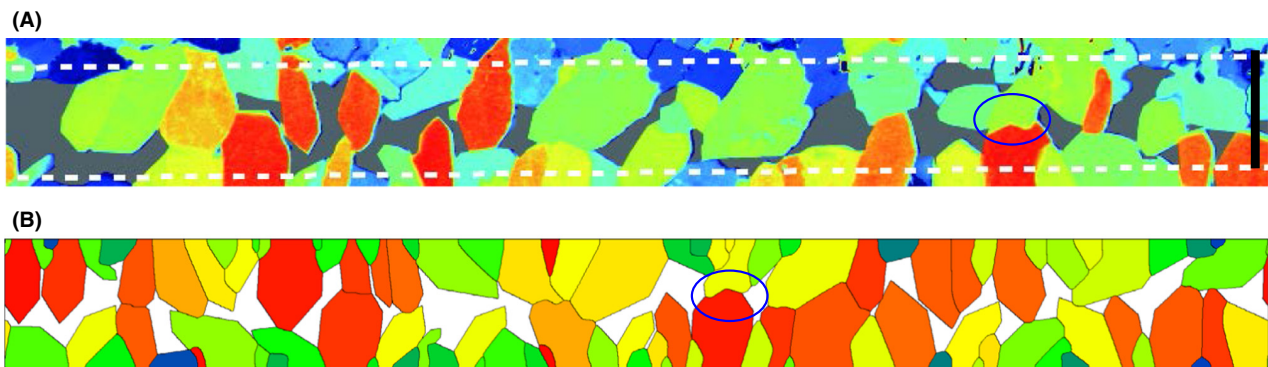


**Fig. 11.** Syntaxial vein sealing (color scale as in Fig. 9): (A) c-axis orientations of partly sealed synthetic vein in metachert sample JU4-4IK with grain size 140 μm from previous study (image reproduced from Fig. 7D in Okamoto & Sekine (2011) with permission), pore space: gray, black scale bar: 0.3 mm. (B) Simulation results, pore space in white color.
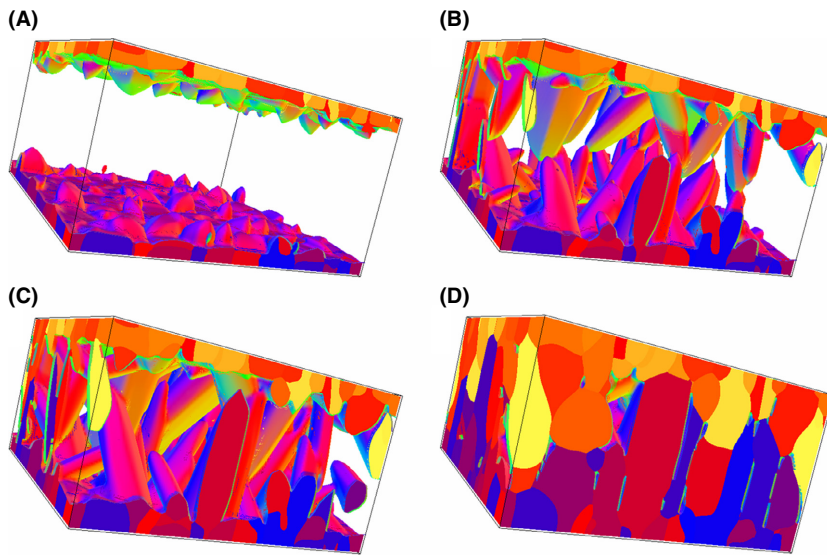
**Fig. 12.** (A–D) 3D simulation of fracture sealing with initial aperture of 80 μm (grid size: 150 × 150 × 80, $S$ = 3.9) and an average grain size of 7 μm (quartz surface in fracture rendered according to surface normal; grains at domain boundaries shown in different color). After a longer initiation period, fast needle growth sets in and creates many crystal bridges. During the four time steps (at $t$ = 0.3, 1.6, 2.9 and 10.3 days) porosity decreases to ~2% at the final stage (D).

orientation distribution in one simulation to describe preferentially subnormal oriented starting grains, resulting in a much better agreement thereafter (#3 in Fig. 10B). When analyzing the 3D simulation (#4 in Fig. 10B), which was adapted to the metachert grain size, no such mechanism is necessary to explain the initial high texture index. To reduce the fluctuations, five 2D scans at different slices of the simulation box were averaged to give the results in Fig. 10B (red circles). The major characteristics of textural evolution are reproduced by the 3D simulation well.

As a simplified model of the geological process under consideration, we reproduced the syntaxial sealing of the synthetic hydrothermal vein from both sides of the open space. An experimental microstructure is given in Fig. 11A for the metachert sample (Okamoto & Sekine 2011), with the initial rock wall boundary indicated as dashed line. An example for a simulated fracture filling in 2D shows Fig. 11B at a time step, where the remaining liquid space is comparable to the experiment. As the width of the slit aperture cut into the rock material is large compared to the average grain size, grain orientations on upper and lower parts of the 'fracture' are not correlated and thus were chosen independently in the simulation. This may be different in naturally occurring cracks, which would leave grains with identical orientations on both sides. Although the simulation was performed in 2D, many details appear similar: Strongly misaligned grains (blue) are quickly overgrown in the competition process. Even the short distance of the vein aperture (300 μm) is sufficient to produce a grain fabric in the fracture with dominating c-axis angles from 45° to 90°, similar to the results of the hydrothermal growth process. When subnormal oriented grains (forming a sharp tip) impinge on their counterparts during vein closure, characteristic wavy grain boundaries are formed at several places. An example in which the encountering

grains have similar orientations in experiment and simulation is indicated by ovals in Fig. 11. These structures would be recognizable in the completely sealed vein structure and could be used as a marker for the boundary between upper and lower part.

Figure 12 shows four time steps of a 3D sealing simulation for a smaller fracture with aperture width of 80 μm and accordingly reduced average grain size of 7 μm. This was done to reduce the computational costs. The simulation starts with a longer initial phase of rest with low mineral mass accretion, in which mainly the grain facets are formed (Fig. 12A). The retardation can be explained by the small grain size leading to a higher average interface curvature, which is equivalent to a negative driving force. Thereafter, the well-aligned crystals finally protrude into the open space and grow fast in the form of quartz needles (Fig. 12B), and finally bridge the gap with an interlocking structure. Complete hydraulic sealing appears here at $t$ = 10.3 days (Fig. 12D), with a remnant porosity of 2%. With the approximation of a constant supersaturation assumed in the simulation, this sealing time must be regarded as a lower limit, as in the late stage of growth, the reduced fluid-transport capability must be taken into account.

## CONCLUSIONS

This study shows how a general PFM can be adapted to a geologically relevant mineralization process. A major goal was to find reliable interface and bulk parameters necessary to capture the morphological evolution of the polycrystalline quartz system. Methods were developed to supplement existing thermodynamic and kinetic results by calibration with specific experimental data. When configured with the values given in this study, the model is able to represent

experimental hydrothermal quartz growth at high temperatures of about 400°C and high pressures of 30 MPa. For different ($p$, $T$) conditions, thermodynamic parameters such as driving force can be easily adapted from literature, whereas the actual growth shapes might change, which additionally requires detailed experiments. The following modeling steps are important to quantitatively capture quartz growth and have not been applied in combination in previous numerical studies of vein growth:

- The solid–liquid interface energies $\gamma_{sl}$ for all exhibited facets have been adapted to best approximate the equilibrium crystal shape (Wulff shape). In the model, the $z$ facet ($\{10\text{–}11\}$) energy was chosen as a reference for interface energy, and all other facet energies defined via the capillary anisotropy function.
- Absolute growth rates depending on the degree of saturation and temperature were defined to represent precipitation kinetics of quartz. Independently, the relative growth rates for all facets were chosen in form of the kinetic anisotropy. In our case, we analyzed the shapes of free grown needle crystals to estimate their values and found facet-specific rates, which compare well to results from other experimental studies. In addition, we defined fast growth rates for noneuhedral directions, which in the simulation favors quartz crystals aligned normal to the boundary.
- The driving force for crystallization, corresponding to the difference of free energies of solid and liquid phase, was determined, and it controls whether silica is precipitated or dissolved. Microstructure and overall growth rate depend intricately on the driving force, which is a function of the supersaturation – assumed as constant in this work – and also depends on the interfacial energy between liquid and crystal, which changes with the local geometry.

In the quartz veins examined here, crystal aggregates evolve by interaction, starting as epitaxial overgrowth of the rock fabric. This growth competition process leads to the formation of a crystallographic preferred orientation and texture evolution, which closely resembles the hydrothermal experiment. As a consequence from the comparison of simulation and experimental results, we propose the scaled grain number and the $V$-index as appropriate measures of validation. It was found that both parameters plotted as a function of the scaled distance from the initial wall are very sensitive to changes in the growth model parameters, variance of grain sizes, and the existence of a predominant texture in the rock matrix.

A strong dependency of morphology on the driving force has been found in the simulations: Whereas high supersaturation leads to more contiguous polycrystalline growth fronts, low supersaturation favors isolated growth of quartz needles and increases orientation selection. The predictions possible with this model might help to unravel aspects of the formation of vein microstructures and the estimation of growth conditions. For the late stages of vein sealing, when pore spaces are filled, transport by flow and diffusion will be taken into account in future work.

## REFERENCES

Ankit K, Nestler B, Selzer M, Reichardt M (2013) Phase-field study of grain boundary tracking behavior in crack-seal microstructures. *Contributions to Mineralogy and Petrology*, **166**, 1709–23.

Blum P, Mackay R, Riley MS, Knight JL (2005) Performance assessment of a nuclear waste repository: upscaling coupled hydro-mechanical properties for far-field transport analysis. *International Journal of Rock Mechanics and Mining Sciences*, **42**, 781–92.

Blum P, Mackay R, Riley MS (2009) Stochastic simulations of regional scale advective transport in fractured rock masses using block upscaled hydro-mechanical rock property data. *Journal of Hydrology*, **369**, 318–25.

Bons A-J, Bons PD (2003) The development of oblique preferred orientations in zeolite films and membranes. *Microporous and Mesoporous Materials*, **62**, 9–16.

Bons PD (2000) The formation of veins and their microstructures. In: *Stress, Strain and Structure, A Volume in Honour of W D Means* (eds Jessell MW, Urai JL), *Journal of the Virtual Explorer*, **2**. online. Available from: http://www.virtual explorer.com.au/article/2000/7/veins-and-their-microstructures/index.html.

Bons PD (2001) Development of crystal morphology during unitaxial growth in a progressively widening vein: I. The numerical model. *Journal of Structural Geology*, **23**, 865–72.

Bons PD, Elburg MA, Gomez-Rivas E (2012) A review of the formation of tectonic veins and their microstructures. *Journal of Structural Geology*, **43**, 33–62.

Choudhury A, Nestler B (2012) Grand-potential formulation for multicomponent phase transformations combined with thin-

interface asymptotics of the double-obstacle potential. *Physical Review E*, **85**, 021602.

Cox SF (2005) Coupling between deformation, fluid pressures, and fluid flow in ore-producing hydrothermal systems at depth in the crust. In: *Economic Geology 100th Anniversary Volume 1905–2005* (eds Hedenquist JW, Thompson JFH, Goldfarb RJ, Richards JP), pp. 39–75. Society of Economic Geologists, Littleton, CO.

Cox SF, Etheridge MA (1983) Crack-seal fibre growth mechanisms and their significance in the development of oriented layer silicate microstructures. *Tectonophysics*, **92**, 147–70.

Dijk P, Berkowitz B (1998) Precipitation and dissolution of reactive solutes in fractures. *Water Resources Research*, **34**, 457–70.

Dove PM, Han N (2007) Kinetics of mineral dissolution and growth as reciprocal microscopic surface processes across chemical driving force. *AIP Conference Proceedings*, **916**, 215.

Durney DW, Ramsay JG (1973) Incremental strains measured by syntectonic crystal growths. In: *Gravity and Tectonics* (eds De Jong KA, Scholten R), pp. 67–96. John Wiley & Sons, New York.

Fisher DM, Brantley SL (1992) Models of quartz overgrowth and vein formation: deformation and episodic fluid flow in an ancient subduction zone. *Journal of Geophysical Research*, **97** (B13), 20043–61.

Fournier R, Potter RW (1982) An equation correlating the solubility of quartz in water from 25° to 900°C at pressures up to 10000 bars. *Geochimica et Cosmochimica Acta*, **46**, 1969–73.

Gale JFW, Lander RH, Reed RM, Laubach SE (2010) Modeling fracture porosity evolution in dolostone. *Journal of Structural Geology*, **32**, 1201–11.

Garcke H, Nestler B, Stoth B (1998) On anisotropic order parameter models for multi-phase systems and their sharp interface limits. *Physica D: Nonlinear Phenomena*, **115**, 87–108.

Hecht U, Gránásy L, Pusztai T, Böttger B, Apel M, Witusiewicz V, Ratke L, De Wilde J, Froyen L, Camel D, Drevet B, Faivre G, Fries SG, Legendre B, Rex S (2004) Multiphase solidification in multicomponent alloys. *Materials Science and Engineering: R*, **46**, 1–49.

Hilgers C, Tenthorey E (2004) Fracture sealing of quartzite under a temperature gradient: experimental results. *Terra Nova*, **16**, 173–8.

Hilgers C, Dilg-Gruschinski K, Urai JL (2004) Microstructural evolution of syntaxial veins formed by advective flow. *Geology*, **32**, 261–4.

Hilgers C, Urai JL (2002) Experimental study of syntaxial vein growth during lateral fluid flow in transmitted light: first results. *Journal of Structural Geology*, **24**, 1029–43.

Hilgers C, Koehn D, Bons PD, Urai JL (2001) Development of crystal morphology during unitaxial growth in a progressively widening vein: II. Numerical simulations of the evolution of antitaxial fibrous veins. *Journal of Structural Geology*, **23**, 873–85.

Hiraga T, Nishikawa O, Nagase T, Akizuki M, Kohlstedt DL (2002) Interfacial energies for quartz and albite in pelitic schist. *Contributions to Mineralogy and Petrology*, **143**, 664–72.

Holland M, Urai JL (2010) Evolution of anastomosing crack–seal vein networks in limestones: insight from an exhumed high-pressure cell, Jabal Shams, Oman Mountains. *Journal of Structural Geology*, **32**, 1279–90.

Holness MB (1993) Temperature and pressure dependence of quartz-aqueous fluid dihedral angles: the control of adsorbed H2O on the permeability of quartzites. *Earth and Planetary Science Letters*, **117**, 363–77.

Hubert J, Emmerich H, Urai JL (2009) Modelling the evolution of vein microstructure with phase-field techniques – a first look. *Journal of Metamorphic Geology*, **27**, 523–30.

IAPWS (2007) Revised Release of the IAPWS Industrial Formulation 1997 for the Thermodynamic Properties of Water and Steam. Available from: http://www.iapws.org.

Ihinger PD, Zink SI (2000) Determination of relative growth rates of natural quartz samples. *Nature*, **404**, 865–9.

Iwasaki H, Iwasaki F, Yokokawa H, Kurashige M, Oba K (2002) Computer simulation of growth process in synthetic quartz crystals grown from X-bar, Y-bar and rectangular Z-plate seeds. *Journal of Crystal Growth*, **234**, 711–20.

Iwasaki H, Iwasaki F (1995) Morphological variations of quartz crystals as deduced from computer experiments. *Journal of Crystal Growth*, **151**, 348–58.

Koehn D, Bons PD, Hilgers C, Passchier CW (2001) Animations of progressive fibrous vein and fringe formation. *Journal of the Virtual Explorer*, **4**, 25–30.

Lander RH, Larese RE, Bonnell LM (2008) Toward more accurate quartz cement models: the importance of euhedral versus noneuhedral growth rates. *AAPG Bulletin*, **92**, 1537–63.

Lee Y-J, Morse JW (1999) Calcite precipitation in synthetic veins: implications for the time and fluid volume necessary for vein filling. *Chemical Geology*, **156**, 151–70.

Lee Y-J, Morse JW, Wiltschko DV (1996) An experimentally verified model for calcite precipitation in veins. *Chemical Geology*, **130**, 203–15.

de Leeuw NH (2008) Computer simulations of surfaces and interfaces: a case of study of the hydration and dissolution of α-quartz SiO₂. In: *Computer Methods in Mineralogy and Geochemistry* (eds Prieto M, Brime C), Seminarios de la Sociedad Española de Mineralogía. *Seminarios SEM*, **4**, 66–102.

Li X, Huang H, Meakin P (2008) Level set simulation of coupled advection-diffusion and pore structure evolution due to mineral precipitation in porous media. *Water Resources Research*, **44**, W12407.

Moelans N, Blanpain B, Wollants P (2008) An introduction to phase-field modeling of microstructure evolution. *Calphad*, **32**, 268–94.

Nestler B, Wendler F, Selzer M, Stinner B, Garcke H (2008a) Phase-field model for multiphase systems with preserved volume fractions. *Physical Review E*, **78**, 1–7.

Nestler B, Reichardt M, Selzer M (2008b) Massive multi-phase-field simulations: methods to compute large grain system. In: *Proceedings of the 11th international conference on aluminium alloys*, Aachen, Germany (eds Hirsch J, Skrotzki B, Gottstein G), pp. 1251–1255. Wiley-VCH, Weinheim.

Nestler B, Garcke H, Stinner B (2005) Multicomponent alloy solidification: phase-field modeling and simulations. *Physical Review E*, **71**, 041609.

Nollet S, Hilgers C, Urai JL (2006) Experimental study of polycrystal growth from an advecting supersaturated fluid in a model fracture. *Geofluids*, **6**, 185–200.

Nollet S, Urai JL, Bons PD, Hilgers C (2005) Numerical simulations of polycrystal growth in veins. *Journal of Structural Geology*, **27**, 217–30.

Okamoto A, Sekine K (2011) Textures of syntaxial quartz veins synthesized by hydrothermal experiments. *Journal of Structural Geology*, **33**, 1764–75.

Okamoto A, Saishu H, Hirano N, Tsuchya N (2010) Mineralogical and textural variation of silica minerals in hydrothermal flow-

through experiments: implications for quartz vein formation. *Geochimica et Cosmochimica Acta*, **74**, 3692–706.

Okamoto A, Tsuchiya N (2009) Velocity of vertical fluid ascent within vein-forming fractures. *Geology*, **37**, 563–6.

Oliver NHS, Bons PD (2001) Mechanisms of fluid flow and fluid-rock interaction in fossil metamorphic hydrothermal systems inferred from vein-wallrock patterns, geometry and microstructure. *Geofluids*, **1**, 137–62.

Oliver NHS (1996) Review and classification of structural controls on fluid flow during regional metamorphism. *Journal of metamorphic Geology*, **14**, 477–92.

Ostapenko GT, Mitsyuk BM (2006) Asymmetry of growth and dissolution on basal, minor rhombohedral and prism faces of quartz. *Journal of Crystal Growth*, **294**, 330–8.

Parks GA (1984) Surface and interfacial free energies of quartz. *Journal of Geophysical Research: Solid Earth*, **89**(B6), 3997–4008.

Ramsay J (1980) The crack-seal mechanism of rock deformation. *Nature*, **284**, 135–9.

Rimstidt JD, Barnes HL (1980) The kinetics of silica-water reactions. *Geochimica et Cosmochimica Acta*, **44**, 1683–99.

Sekerka RF (2005) Equilibrium and growth shapes of crystals: how do they differ and why should we care? *Crystal Research and Technology*, **40**, 291–306.

Steefel C, Depaolo D, Lichtner P (2005) Reactive transport modeling: an essential tool and a new research approach for the Earth sciences. *Earth and Planetary Science Letters*, **240**, 539–58.

Suzuki T, Kasahara H (2010) Determination of the specific surface free energy of natural quartz crystals using measurement of contact angle of liquid droplets. *Crystal Research and Technology*, **45**, 1305–8.

Urai JL, Williams PF, van Roermund HLM (1991) Kinematics of crystal growth in syntectonic fibrous veins. *Journal of Structural Geology*, **13**, 823–36.

Walton M (1960) Molecular diffusion rates in supercritical water vapor estimated from viscosity data. *American Journal of Science*, **258**, 385–401.

Wendler F, Mennerich C, Nestler B (2011) A phase-field model for polycrystalline thin film growth. *Journal of Crystal Growth, Elsevier*, **327**, 189–201.

Wendler F, Becker JK, Nestler B, Bons PD, Walte NP (2009) Phase-field simulations of partial melts in geological materials. *Computers & Geosciences*, **35**, 1907–16.

Yoon H, Valocchi AJ, Werth CJ, Dewers T (2012) Pore-scale simulation of mixing-induced calcium carbonate precipitation and dissolution in a microfluidic pore network. *Water Resources Research*, **48**, W02524.

## APPENDIX A: GROWTH EQUATION

Writing the phase-field kinetic equation Eq. (5) in the limit of a sharp interface between phase α and β, one gets the local growth velocity $v_n$ as function of surface normal vector $\hat{n}$,

$$v_n = \omega_{\alpha\beta}^0(\hat{n})\left(f(p, T, \mathbf{c})|_\alpha^\beta - \gamma_{\alpha\beta}(\hat{n})\kappa\right), \qquad (A1)$$

where κ is the mean curvature and $f(p, T, \mathbf{c})|_\alpha^\beta = f_\alpha(p, T, \mathbf{c}) - f_\beta(p, T, \mathbf{c})$ is the driving force. Here, the kinetic coefficient for the α–β interface $\omega_{\alpha\beta}^0$ includes the kinetic anisotropy function $a_{\alpha\beta}^{\mathrm{kin}}(\hat{n})$ as a modulating factor, and the surface ten-

sion, the capillary anisotropy $a_{\alpha\beta}^{\mathrm{cap}}(\hat{n})$. It follows, that for solid–liquid equilibrium ($v_n = 0$), only $a_{\alpha\beta}^{\mathrm{cap}}(\hat{n})$ defines evolution by minimizing surface energy, hence creating the Wulff shape. On the other hand, for larger driving forces, the expanding Wulff shape created by the bracketed term on the r.h.s. of Eq. (A1) is modulated by the kinetic anisotropy function. Then, the velocity is given by $v_n = \omega_{\alpha\beta}^0 \cdot a_{\alpha\beta}^{\mathrm{kin}}(\hat{n}) \cdot a_{\alpha\beta}^{\mathrm{cap}}(\hat{n}) \cdot f(p, T, \mathbf{c})|_\alpha^\beta$.

## APPENDIX B: MATHEMATICAL FORM OF THE ANISOTROPY FUNCTIONS

The capillary anisotropy for the Wulff shape is calculated by finding the maximum inner product of surface normal and all vertex vectors $\boldsymbol{\eta}_k^{\mathrm{sl}}$ of the crystal polyhedron,

$$a_{\mathrm{sl}}^{\mathrm{cap}}(\hat{n}) = \max k\{\hat{n}\boldsymbol{\eta}_k^{\mathrm{sl}}\}, \ (k = 1 \ldots K), \qquad (A2)$$

(Wendler *et al.* 2011; Ankit *et al.* 2013). In Eq. (A2), $K$ denotes the number of vertex vectors and $\max_k \{\ldots\}$, the maximum value of all arguments in braces. Similar to the surface energy in the Kossel crystal model, the resulting energy shape is composed of circular arcs (spheres in 3D), with facets appearing at the cusp locations (see Fig. 4C,D). Differently oriented crystals are produced by rotating the vertex vectors $\boldsymbol{\eta}_k^{\mathrm{sl}}$, which are given in Appendix C in the reference coordinate system.

To realize an adjustable growth rate for non-euhedral crystal directions, the following modification of Eq. (A2) for the kinetic anisotropy was developed,

$$\begin{aligned} a_{\alpha\beta}^{\mathrm{kin}}(\hat{n}) &= \left(1 + \delta\left(\cdot \max_k\left\{\hat{n}\boldsymbol{\eta}_k^{\alpha\beta}\right\} - \max_{k-1}\left\{\hat{n}\boldsymbol{\eta}_k^{\alpha\beta}\right\}\right)\right) \\ &\quad \cdot \max_k\left\{\hat{n}\boldsymbol{\eta}_k^{\alpha\beta}\right\}. \end{aligned}$$

$$(A3)$$

Here, $\max_{k-1} \{\ldots\}$ denotes the second largest argument in the braces. The effect of the modulating prefactor in brackets in Eq. (A3) is to leave the values at the facet orientations unchanged – that is the cusp positions in the gamma-plot – but shift all values in between proportionally along the radial direction (from the dashed red curve to the solid red curve in Fig. 4D). The strength of the prefactor in our simulations is adapted by the constant δ = 85 to give the desired ratio of $c$- to $z$-facet velocity of $v_c$: $v_z = 8.6{:}1$.

## CRYSTAL SHAPE VECTORS

The capillary anisotropies in Eqs (A2) and (A3) are defined by the vertex vectors of the Wulff shape. The angle between the $m$- and $c$-crystal faces of 51.78° enters here. For the 2D

**Table 6.** The 14 polyhedral vertex vectors of the Wulff shape (3D).

| Upper part ($z > 0$) | | | Lower part ($z < 0$) | | |
|---|---|---|---|---|---|
| x | y | z | x | y | z |
| 0 | 0 | 1.6165 | 0 | 0 | −1.6165 |
| 0.4536 | 0.7856 | 0.6187 | 0.4536 | 0.7856 | −0.6187 |
| 0.4536 | −0.7856 | 0.6187 | 0.4536 | −0.7856 | −0.6187 |
| −0.4536 | 0.7856 | 0.6187 | −0.4536 | 0.7856 | −0.6187 |
| −0.4536 | −0.7856 | 0.6187 | −0.4536 | −0.7856 | −0.6187 |
| 0.9072 | 0 | 0.6187 | 0.9072 | 0 | −0.6187 |
| −0.9072 | 0 | 0.6187 | −0.9072 | 0 | −0.6187 |

**Table 7.** The 32 polyhedral vertex vectors of the kinetic Wulff shape (3D).

| Upper part ($z > 0$) | | | Lower part ($z < 0$) | | |
|---|---|---|---|---|---|
| x | y | z | x | y | z |
| 0 | 0 | 1.6165 | 0 | 0 | −1.6165 |
| 0.2204 | −0.1273 | 1.4549 | 0.2204 | 0.1273 | −1.4549 |
| −0.2204 | −0.1273 | 1.4549 | −0.2204 | 0.1273 | −1.4549 |
| 0 | 0.2546 | 1.4549 | 0 | −0.2546 | −1.4549 |
| 0.0262 | 0.3 | 1.3971 | 0.0262 | −0.3 | −1.3971 |
| −0.0262 | 0.3 | 1.3971 | −0.0262 | −0.3 | −1.3971 |
| 0.2467 | −0.1727 | 1.3971 | 0.2467 | 0.1727 | −1.3971 |
| −0.2467 | −0.1727 | 1.3971 | −0.2467 | 0.1727 | −1.3971 |
| 0.2729 | −0.1273 | 1.3971 | 0.2729 | 0.1273 | −1.3971 |
| −0.2729 | −0.1273 | 1.3971 | −0.2729 | 0.1273 | −1.3971 |
| 0.1732 | 0.3 | 1.2355 | 0.1732 | 0.3 | −1.2355 |
| 0.1732 | −0.3 | 1.2355 | 0.1732 | −0.3 | −1.2355 |
| −0.1732 | 0.3 | 1.2355 | −0.1732 | 0.3 | −1.2355 |
| −0.1732 | −0.3 | 1.2355 | −0.1732 | −0.3 | −1.2355 |
| 0.3464 | 0 | 1.2355 | 0.3464 | 0 | −1.2355 |
| −0.3464 | 0 | 1.2355 | −0.3464 | 0 | −1.2355 |

simulations, the following six polygonal vertex vectors for the Wulff shape

$$\boldsymbol{\eta}^{sl}_{1,2} = \begin{pmatrix} 0 \\ \pm 1/\cos(51.78°) \end{pmatrix} = \begin{pmatrix} 0 \\ \pm 1.6163 \end{pmatrix},$$
$$\boldsymbol{\eta}^{sl}_{3,\ldots 6} = \begin{pmatrix} \pm \sin(51.78°) \\ \pm \cos(51.78°) \end{pmatrix} = \begin{pmatrix} \pm 0.7856 \\ \pm 0.6187 \end{pmatrix} \quad (A4)$$

and the six polygonal vertex vectors for the kinetic Wulff shape were used.

$$\boldsymbol{\eta}^{sl}_{1,2} = \begin{pmatrix} 0 \\ \pm 1.6163 \end{pmatrix}, \quad \boldsymbol{\eta}^{sl}_{3,\ldots 6} = \begin{pmatrix} \pm 0.3 \\ \pm 1.2354 \end{pmatrix}. \quad (A5)$$

In 3D, the quartz shape is a hexagonal prism capped by two pyramids (c-axis parallel to z coordinate direction).

The Wulff shape contains 14 vectors, calculated by intersection of the respective facets at specified distances (Table 6). Due to the nonequivalent pyramidal z and r faces found in the analysis of the crystal shapes, the kinetic anisotropy shape then comprises a set of 32 vertex vectors (Table 7).

# GEOFLUIDS

## CONTENTS